Stony Brook University

Microstructure Investigation of Thermoelectric Materials

A Dissertation Presented

by

Juan Zhou

to

The Graduate School

In Partial Fulfillment of the

Requirements

for the Degree of

Doctor of Philosophy

in

Materials Science and Engineering

Stony Brook University

December 2010

Stony Brook University

The Graduate School

Juan Zhou

We, the dissertation committee for the above candidate for the Doctor of Philosophy degree, hereby recommend acceptance of the dissertation.

Qiang Li - Dissertation Advisor
Scientist, Department of Condensed Matter Physics and Materials Science
Brookhaven National Laboratory
Adjunct Professor, Department of Materials Science and Engineering
Stony Brook University

Dilip Gersappe - Chairperson of Defense
Associate Professor, Department of Materials Science and Engineering
Stony Brook University

Lijun Wu
Ph. D., Science Associate, Department of Condensed Matter Physics and Materials Science
Brookhaven National Laboratory

Jing Tao
Ph. D., Assistant Scientist, Department of Condensed Matter Physics and Materials Science
Brookhaven National Laboratory

This dissertation is accepted by the Graduate School.

Lawrence Martin
Dean of the Graduate School

Abstract of the Dissertation

Microstructure Investigation of Thermoelectric Materials

By

Juan Zhou

Doctor of Philosophy

in

Materials Science and Engineering

Stony Brook University

2010

Thermoelectric materials can convert heat directly into electricity and hence may play an important role in the future of energy conversion. In the last decade, the performance of thermoelectric materials has been enhanced substantially. Most of the progress is obtained through a control of the microstructure of a material. Especially, nanometer scale substructures present in the materials are thought to play a critical role for the significant reduction of lattice thermal conductivity and enhancement of figure of merit. A comprehensive understanding of the role of the micro- and nano-scale structural features on the electron and phonon transport would facilitate the design of more efficient materials. To achieve this, an accurate description of the detailed structures of these features, their formation mechanisms, and interactions with the matrix is necessary. Such a work is also helpful for establishing the

correlation between the microstructures, materials synthesis and thermoelectric properties.

Advanced analytical tools such as X-ray diffractometry (XRD), scanning electron microscopy (SEM), and transmission electron microscopy (TEM) etc enable probing the material structures at different length scales, and therefore help to give a comprehensive and detailed description of many interesting structural features of a material. In this work, microstructure investigation of two kinds of most promising thermoelectric materials has been conducted via these tools to uncover the underlying structural mysteries which lead to their superior thermoelectric properties.

$AgPb_{18}SbTe_{20}$ ($(PbTe)_{1-x}(AgSbTe_2)_x$ with x ~ 0.05 or LAST-18) is the material from which the highest figure of merit has been obtained in all known bulk thermoelectric materials. For this material, high resolution TEM imaging and structure analysis have been intensively employed to uncover the structural details of the nanoprecipitates prevalent in the single crystal samples to the atomistic scale. The underlying mechanism for the nucleation of the nanoprecipitates and their interactions with the matrix lattice are also discussed through the coordinated image simulation and large scale density functional theoretical (DFT) calculations.

$CeFe_4Sb_{12}$, a p-type filled skutterudite compound, has been prepared in our group through a novel non-equilibrium synthesis method combining melt spinning and spark plasma sintering (SPS). Remarkable improvements in both electrical and thermal transport properties have been achieved in them when compared to those of

the same materials prepared by the conventional way. A comparative microstructure study of the $CeFe_4Sb_{12}$ bulk samples prepared by both the non-equilibrium and conventional methods has been carried out in order to understand the structural origins for the substantially improved thermoelectric properties in the non-equilibrium synthesized samples.

Table of Contents

List of Tables

List of Figures

Acknowledgements

First of all, I would like to express my sincerest gratitude to my advisor Dr. Qiang Li for all of his patient and insightful guidance in my work on this dissertation. His attitude towards scientific problems, way of creative thinking, and strong background in both theoretical knowledge and experimental skills give me the best training necessary to accomplish my research work. My future work will also definitely benefit from the training he has given me in his group. Without his generous support and help, this dissertation may not be possible.

I appreciate Dr. Qiang Li, Dr. Dilip Gersappe, Dr. Lijun Wu, and Dr. Jing Tao for serving as my defense committee in their busy schedules.

I deeply appreciate tons of help I got from Dr. Lijun Wu and Dr. Yimei Zhu in the TEM work and Dr. Qing Jie in the thermoelectric materials synthesis and properties measurement work.

I would thank Dr. Jihui Yang and Dr. Xun Shi from General Motors Corporation for supplying part of the samples for this work.

I would thank Mr. Kim Kisslinger, Dr. Chao Ma, Dr. Lihua Zhang, and Dr. Jing Tao for all the warm help in the TEM related work.

Finally, I would like to express my deepest gratitude to my family for their continuous support and trust on me.

1. Introduction

1.1. Thermoelectric basics

Serious concern about worldwide energy crisis and greenhouse effect has driven the demand for alternative energy to reduce our dependence on fossil fuels. Thermoelectrics allow for the direct energy conversion between heat and electricity using thermoelectricity.[1] Thermoelectric (TE) power generators convert heat directly into electricity without hazardous emissions, and thermoelectric refrigerators use electricity for cooling without chlorofluorocarbons (CFCs). Similar to solid state electronic devices, thermoelectric power generators and refrigerators possess several advantages. First, they don't have moving parts, so they are silent in operation and need much less maintenance. Secondly, they don't produce waste in the energy conversion process. Thirdly, they can be processed at micrometer or even at tens of nanometer scaled size, thus can be easily utilized in electronic devices. Consequently, thermoelectric materials and devices have received increasing interest in the last decade and are thought to have the potential to play an important role in the future of energy conversion and utilization. Next, a brief introduction of thermoelectric basics is given, which includes thermoelectric effects, modules and applications.

1.1.1 Thermoelectric effects and modules

The Seebeck and Peltier effects are the two most important thermoelectric effects. They represent the coupling of electrical and thermal currents. Thermoelectric power generators and refrigerators are developed based on these two effects.

The Seebeck effect was named after Thomas Johann Seebeck, who discovered this effect for the first time in 1821.[2] When a temperature gradient ΔT is applied on the two ends of a conductor, electrons (or holes) will diffuse from the hot end to the cold end. The charges build up on the cold end and create an electric field ΔV.

Seebeck coefficient or thermopower S is defined as

$$S = \frac{\Delta V}{\Delta T} \tag{1.1}$$

$S > 0$ if the charge carriers are holes and the materials are called p-type thermoelectric materials. $S < 0$ when the charge carriers are electrons and the materials are called n-type thermoelectric materials.

Peltier described thermal effects at the junctions of dissimilar conductors when an electrical current flows between the materials in 1834.[3] The Peltier effect is expressed as

$$Q = \Pi I \tag{1.2}$$

Here Q is the heat absorption/emission induced at the junctions by the applied current I and Π is the Peltier coefficient.

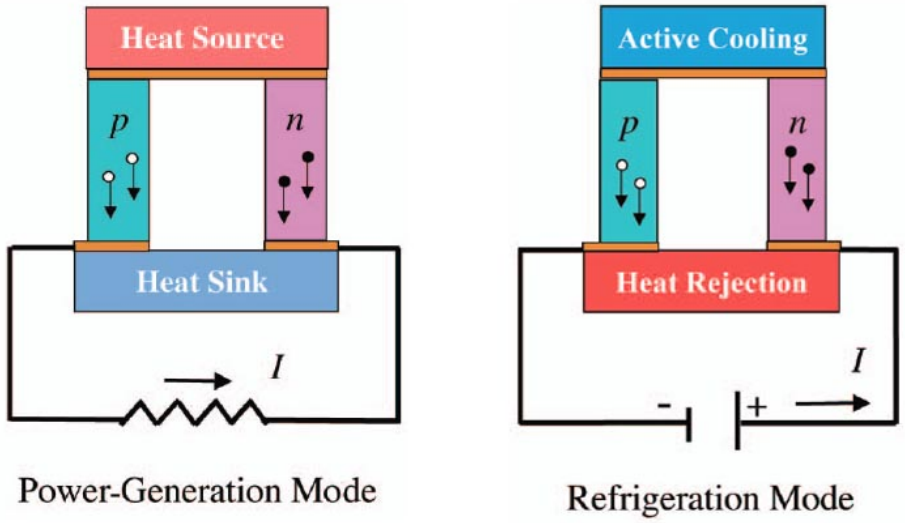

Figure 1.1 Schematics of thermoelectric power generation mode and refrigeration mode.[4]

The schematics of thermoelectric power generation mode and solid-state electronics refrigeration mode are shown in **Figure 1.1**.[4] Thermoelectric power generators operate based on Seebeck effect and can be used to convert waste heat to electricity. Thermoelectric solid state refrigerators work based on Peltier effect to pump heat from the cold to the hot ends.

1.1.2 Thermoelectric applications

Typical thermoelectric applications include supplying power to NASA spacecrafts such as Voyager, Galileo, and Ulysses with radioisotope thermoelectric generators which convert heat released from nuclear decay of radioactive isotopes into electricity.[5] Another important thermoelectric application is the recovery of waste heat produced by automotive vehicles.[6] When a car is running, the surface temperature of some internal pipelines goes very high and a lot of waste heat is produced. Usually for

a typical gasoline fueled internal combustion engine vehicle, only about 25% of the fuel energy is utilized for vehicle mobility and accessories; the remainder 75% is lost in the form of waste heat in exhaust and coolant, as well as friction and parasitic losses. Great fuel economy will be obtained if a portion of the waste heat from automotive industries and other sources like the power factories can be utilized to generate electricity. Thermoelectric refrigeration devices include small solid-state refrigerators, picnic coolers, and climate control seats etc.

1.1.3 Figure of merit

The performance of thermoelectric devices is determined by the efficiency of thermoelectric materials. Finding high efficiency thermoelectric materials has always been a technological objective for realizing widespread thermoelectric applications. The efficiency[7] of a thermoelectric material is measured by a dimensionless quantity - the thermoelectric figure of merit *ZT*

$$ZT = \frac{S^2\sigma}{\kappa}T = \frac{S^2}{\rho(k_e + k_L)}T \qquad (1.3)$$

where S, σ, κ, T stands for the Seebeck coefficient, electrical conductivity, thermal conductivity, and absolute temperature, respectively. The power factor, *PF*, is defined as $PF = S^2\sigma$. The electrical resistivity $\rho = 1/\sigma$. The total thermal conductivity $\kappa = \kappa_e + \kappa_L$, in which κ_e is the electronic thermal conductivity and κ_L is the lattice thermal conductivity. An ideal thermoelectric material should have good electrical properties which result in high power factor $S^2\sigma$ and low thermal conductivity κ.

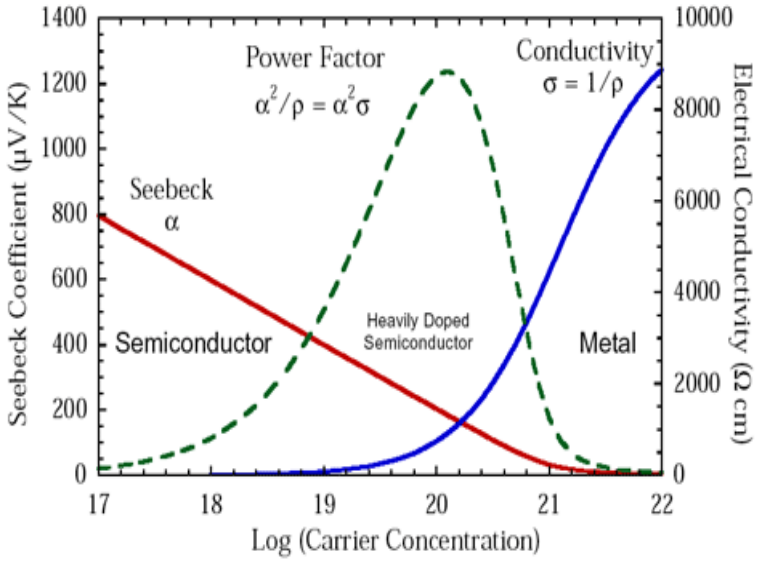

Figure 1.2 Dependence of Seebeck coefficient and electrical conductivity with carrier concentrations.[8]

Theoretically, there is no upper limit for *ZT* values. However, the components in Formula 1.3 except κ_L are related to each other. Usually it is very difficult to control them independently. For example, the variations of Seebeck coefficient *S*, electrical conductivity σ, and power factor $S^2\sigma$ as a function of carrier concentrations are shown in **Figure 1.2**.[8] With the increase of carrier concentrations, Seebeck coefficient decreases while the electrical conductivity increases. For metals, they have high electrical conductivities, but their Seebeck coefficients are too low. Contrarily, insulators have high Seebeck coefficients but very low electrical conductivities. Highest power factor $S^2\sigma$ occurs at an optimal carrier concentration range around 10^{19} – 10^{20} cm^{-3}, which is close to the carrier concentrations of heavily doped semiconductors.

Furthermore, electrical conductivity σ and electronic contribution to thermal conductivity κ_e are related to each other via Wiedemann - Franz law[9],

$$\kappa_e = L\sigma T \tag{1.4}$$

where L = 2.45×10^{-8} WΩK^{-2} is the Lorenz number for metals. Thus, the lattice thermal conductivity κ_L can be conveniently obtained by subtracting κ_e from κ. For degenerate semiconductors, assessment of κ_L in this way can be only an approximation because the precise Lorenz numbers and their temperature dependence are unknown.

1.2. Current status of thermoelectric materials

In a simplified model[10] of one-band materials with constant relaxation time and parabolic bands, *ZT* of three dimensional (*3D*) bulk materials can be given as,

$$Z_{3D}T = \frac{\frac{3}{2}\left(\frac{5F_{3/2}}{3F_{1/2}} - \varsigma^*\right)^2 F_{1/2}}{\frac{1}{B} + \frac{7}{2}F_{5/2} - \frac{25F_{3/2}^2}{6F_{1/2}}} \tag{1.5}$$

Where,

$$F_i = F_i\left(\varsigma^*\right) = \int_0^\infty \frac{x^i dx}{e^{(x-\varsigma^*)} + 1} \tag{1.6}$$

is the Fermi-Dirac function; and

$$\varsigma^* = \varsigma / k_B T \tag{1.7}$$

is the reduced chemical potential.

From Eq. 1.5, we can see that ZT values approximately scale with the so-called B-factor, which is determined by several material-related parameters, and sometimes used to evaluate the performance of a thermoelectric material.

$$B = \gamma \frac{1}{3\pi^2}\left(\frac{2k_B T}{h^2}\right)^{3/2} \sqrt{m_x m_y m_z}\, \frac{k_B^2}{e k_L}\, \mu_x \tag{1.8}$$

$$\mu = \frac{e\tau}{m_i} \tag{1.9}$$

where γ, κ_B, m_i, h, e, μ_x, κ_L, and τ stands for the band degeneracy, Boltzmann constant, effective mass of the carriers in the i^{th} direction, Plank constant, electron charge, carrier mobility along the transport direction, lattice thermal conductivity, and carrier scattering time, respectively.

Accordingly, a potential thermoelectric material should be a heavily doped semiconductor with high band degeneracy γ, large effective mass m, high carrier mobility μ, and low lattice thermal conductivity κ_L. High crystal symmetry such as cubic or hexagonal with a large number of atoms in the unit cell, usually enhances the value of γ.[11] Long scattering times are possible in materials which have small electronegativity differences between the elements. Use of heavy elements with high atomic mass can reduce atomic vibrations and thus reduce κ_L. In many conventional thermoelectric semiconductors, the lattice thermal conductivity κ_L is much larger than electronic part κ_e, so the main challenge is to reduce κ_L. Use of heavy elements can reduce κ_L, while electrical resistivity ρ is usually increased.[12] Alternate strategies that

can effectively reduce κ_L without deteriorating electrical transport significantly are desirable to obtain high *ZT* values in thermoelectric materials.

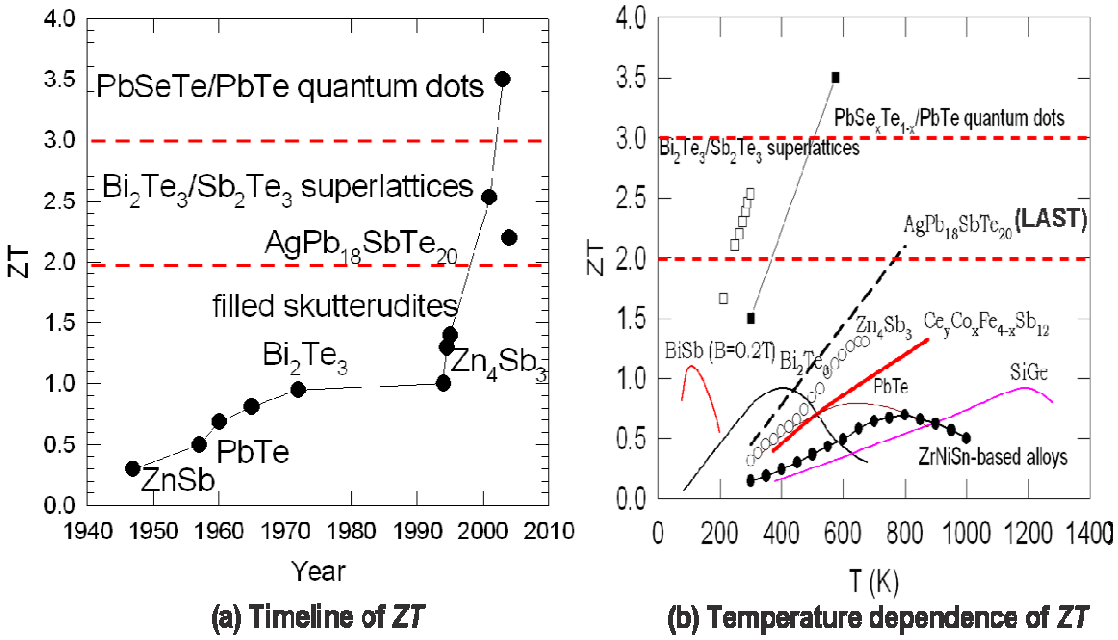

Figure 1.3 (a) Timeline of ZT[13]; (b) Temperature dependence of ZT for several important thermoelectric materials.

ZT values of at least 3 are required in order to compete with traditional power generation and refrigeration methods in efficiency, while most current state-of-the-art thermoelectric materials have their *ZT* values below or around 1. **Figure 1.3a**[13] shows the important thermoelectric materials in different years, from which we can see thermoelectric materials have gone through a very long slow-development history. *ZT* values of practical thermoelectric materials were below 1 for many years. Only several few kinds of thermoelectric materials have been used for practical applications, which are Bi_2Te_3, PbTe, $Si_{1-x}Ge_x$ and their alloys.[14] Bi_2Te_3 and its solid solution $Bi_{2-x}Sb_xTe_3$ and $Bi_2Te_{3-x}Se_x$ are the most efficient materials for cooling with *ZT* values about 1 at 400 K.[7] They have been used for cooling applications such as the

commercially available Peltier coolers. PbTe is used for potential power generation, its maximum *ZT* value is 0.8 at 800 K.[15] $Si_{0.8}Ge_{0.2}$ is superior above 1000 K, which is the thermoelectric material NASA uses on spacecrafts.[16] Due to the low *ZT* values, thermoelectric applications are limited to areas where the efficiency and economy are less important issues than energy availability and reliability, such as NASA deep space probes and cryogenic infrared night vision devices. Further exploration of new thermoelectric materials with improved *ZT* is needed.

Breakthroughs took place in the 1990s not only in the emergence of new thermoelectric materials, but also on the big enhancement in *ZT* values. **Figure 1.3b** shows the temperature dependence of *ZT* values of these materials. New bulk thermoelectric materials demonstrate *ZT* values well above 1.[17-19] More markedly, several materials with quantum dots and superlattice structures even show *ZT* values higher than 3.[20-23]

Two different strategies have been taken to develop promising thermoelectric materials with higher *ZT* values.[24] One strategy is through the development of low-dimensional materials, in which superlattices or quantum dot structures are designed to increase electron density of states (DOS) at the Fermi level by the quantum confinement of electrons, and enhance boundary scattering of phonons to reduce the thermal conductivity.[10, 25-26] It has been thought that the lowest thermal conductivity in crystalline solids is the alloy limit, which is caused by the scattering of phonons by atomic substitutions. However, in the $In_{0.53}Ga_{0.47}As$ film containing

randomly distributed ErAs nanoparticles, a thermal conductivity reduction by almost a factor of 2 below the alloy limit and a corresponding increase in the thermoelectric figure of merit by a factor of 2 have been demonstrated.[27] Very high *ZT* values of 2.4 at 300 K for Bi_2Te_3/Sb_2Te_3 superlattice thin films[22] and 3.5 for PbSeTe/PbTe quantum dots[23] at 600 K have also been obtained.

Although large enhancements in *ZT* values have been observed in various low-dimensional material systems, high performance bulk materials which can work with large heat load and be prepared by volume at low costs are still more desirable for large scale power generation. Therefore, the other strategy has been focused on preparing high efficiency bulk materials. New concepts and crystal structures have been taken in the design and synthesis of high performance bulk thermoelectric materials. These materials are either host materials containing nanoscale substructures[28-30] or obeying the phonon glass/electron crystal (PGEC) paradigm[31].

Nano-engineering has been proven to be an effective way of producing bulk thermoelectric materials with fine-tunable thermoelectric properties. So far, there have been many reports which attribute the significant improvements of *ZT* values to the large reductions in lattice thermal conductivities of materials comprised of nanometer sized grains[32-34] or containing nanoscale substructures[28]. $AgPb_mSbTe_{m+2}$ compounds (also known as $(PbTe)_{1-x}(AgSbTe_2)_x$ or LAST-m) are the most successful examples of high *ZT* bulk thermoelectric materials containing nanoscale inclusions. In 2004, Kanatzidis group first reported that the quaternary n-type degenerate semiconductor

$AgPb_{18}SbTe_{20}$ (LAST-18) exhibited a high *ZT* value of about 2.1 at 800 K, which outperformed all other reported bulk materials.[28] This finding renewed interest in this system. It has also been reported that p-type nanocrystalline $Bi_xSb_{2-x}Te_3$ prepared by high energy ball milling and hot press sintering shows a very high *ZT* value of 1.4 at 373 K.[32] Before this, the highest *ZT* value of bulk $Bi_xSb_{2-x}Te_3$ had remained around 1 for more than 50 years. In spinodal decomposed $PbTe_{0.7}S_{0.3}$, dislocations, boundaries and nanoprecipitates have also been shown to significantly reduce κ_L to only 35% of PbTe and 30% of PbS.[35]

An ideal thermoelectric material should conduct electricity like a crystal but conduct heat like a glass. This is the famous phonon-glass/electron-crystal (PGEC) concept put forward by G. A. Slack in 1995.[31] Typical PGEC thermoelectric materials include filled skutterudites[17-19, 36-43] and Clathrates[44-46], in which independent rattling of the guest atoms in the open cages of the crystal structures results in substantial suppression of the lattice thermal conductivity.

In these materials, $AgPb_mSbTe_{m+2}$ compounds and filled skutterudites represent the two development directions for better bulk thermoelectric materials with one being host materials with nanostructures and the other obeying PGEC paradigm, respectively. In addition, both of them have superior promising thermoelectric properties at intermediate temperatures from 600 to 900 K, which are suitable for waste heat recovery in the automotive industries and solar energy harvesting industries. In our group, they were chosen for systematic material synthesis and

microstructure characterization research. Specific introductions to the research background and our microstructure characterization results of each of the two series of materials are given in Chapter 3 and Chapter 4.

1.3. Role of microstructures and defects on thermoelectric properties

Heat conduction in a thermoelectric material is running through the carriers transport and the lattice vibrations.

$$\kappa_{total} = \kappa_e + \kappa_L \tag{3.1}$$

The existence of different kinds of defects breaks the crystal periodicity in a material, which results in that the heat conduction process through the directional moving of carriers and lattice vibrations is interfered by the defect scattering.

The contribution of carriers to thermal conductivity is related to the electrical conductivity via the Wiedemann - Franz law[9],

$$\kappa_e = L\sigma T \tag{3.2}$$

Heat conduction through the lattice vibrations can be seen as the diffusion of heat-carrying phonons from the hot end to the cold end.[47]

$$k_L = \frac{1}{3} C_v v_s l \tag{3.3}$$

where C_v is the specific heat of the material, v_s is the average diffusion velocity of phonons and l is the mean free path of phonons between two collisions.

When phonons travel through a material, they scatter by several different mechanisms. These are three phonon scattering, phonon-electron scattering, phonon-point defect scattering, and phonon-boundary scattering, respectively. The three-phonon scattering include the normal and Umklapp processes.[48]

Assuming a Debye spectrum for the phonons, and the scattering processes represented by the relaxation rate 1/τ which is inverse to the relaxation time, Callaway[49] gave the formula below for the calculation of κ_L as

$$k_L = \frac{k_B}{2\pi^2 v_S}\left(\frac{k_B T}{\mathrm{h}}\right)^3 \int_0^{\theta_D/T} \tau_c(x)\frac{x^4 e^x}{(e^x-1)^2} \tag{3.4}$$

$$x = \mathrm{h}\omega / k_B T \tag{3.5}$$

$$\omega = k_B T / \mathrm{h} \tag{3.6}$$

where, k_B is the Boltzmann constant, θ_D is the Debye temperature, h is the reduced Planck's constant, ω is the phonon frequency, τ_c is the relaxation time, and T is the absolute temperature.

The combined relaxation rate $1/\tau_c$ is a sum of the relaxation rates due to all kinds of scattering processes.

$$\tau_c^{-1} = \tau_{ph}^{-1} + \tau_B^{-1} + \tau_{PD}^{-1} + \tau_e^{-1} \tag{3.7}$$

where τ_{ph}, τ_B, τ_{PD}, and τ_e are the relaxation time for the phonon-phonon scattering, boundary scattering, point defect scattering, and phonon-electron scattering, respectively.[49]

The normal process (N-process) does not contribute much for the heat conduction. The Umklapp process (U-process) varies with ω^2, and dominates at high frequency. τ_U is given by:

$$\tau_U^{-1} = 2\gamma^2 \frac{k_B T}{\mu V_0} \frac{\omega^2}{\omega_D} \tag{3.8}$$

where γ is the Grüneisen parameter, μ is the shear modulus, V_0 is the volume per atom, and ω_D is the Debye frequency.

The relaxation rate of boundary scattering is independent of the phonon frequency and temperature. It is given by dividing the phonon velocity v_s by the average grain size d of a polycrystalline thermoelectric material.

$$\tau_B^{-1} = v_s / d \tag{3.9}$$

If the size of the defects is much smaller than the phonon wavelength, the resulting defect scattering is called point-defect scattering.

$$\tau_{PD}^{-1} = \frac{V}{4\pi v_s^3} \omega^4 \sum f_i \left(\frac{\overline{m} - m_i}{\overline{m}} \right)^2 \tag{3.10}$$

where V is the volume per atom, m_i is the atom mass, f_i is the content of atoms with mass m_i, $\overline{m}$ is the average atom mass. The inversion of τ_{PD} is proportional to ω^4.

The corresponding relaxation time for phonon-electron scattering is given as:

$$\tau_{ph-e}^{-1} = \frac{n_e \varepsilon \omega}{\rho V^2 k_B T} \sqrt{\frac{\pi m^* V^2}{2 k_B T}} \exp\left\{ -\frac{m^* V^2}{2 k_B T} \right\} \tag{3.11}$$

where n_e is the concentration of conduction electrons, ε is the deformation potential, ρ is the mass density and m^* is the effective mass of electrons. For good thermoelectric materials, which are usually highly doped semiconductors, the contribution to thermal conductivity by phonon-electron scattering is usually negligible.

Heat conduction in solids involves all of these scattering mechanisms and they can sometimes individually dominate at different temperature ranges. At low temperatures, the boundary process usually dominates the phonon scattering. At intermediate temperatures, the point defect scattering usually dominates. At high temperatures, the Umklapp phonon-phonon scattering usually dominates.

At room temperature, the wavelength of carriers is usually several tens nanometers, which is more than ten times larger than that of phonons. Imperfect interfaces, boundaries, and strains caused by misfit between matrix and nanostructures or other defects can preferentially scatter phonons much stronger than their effects on carrier transport.

κ_L is a relatively independent parameter in **Formula 1.3** for calculation of *ZT* values. One of the objectives of engineering better thermoelectric materials would be reducing κ_L of them. Currently, most of the enhancements in *ZT* values have been obtained by effectively suppressing κ_L. The phonon scattering processes are sensitive to the microstructure of a material. Solid solution alloying enhances phonon scattering and reduces κ_L through the introduction of point defects.[13, 50] Extensive efforts have been focused on reducing grain size of a polycrystalline material to enhance boundary

scattering and minimize κ_L.[51-52] For filled skutterudites and clathrates, void filling significantly suppresses κ_L due to the enhanced point defect scattering and resonant phonon scattering.[17-18, 36, 39]

2. Investigation methods

In this work, comprehensive microstructure studies have been carried out on LAST-18 single crystals and non-equilibrium synthesized filled skutterudite $CeFe_4Sb_{12}$ polycrystals using synchrotron white beam X-ray topography (SWBXT), X-ray powder diffraction (XRD), scanning electron microscopy (SEM), transmission electron microscopy (TEM), energy dispersive spectroscopy (EDS) and geometric phase analysis (GPA) software.

2.1 Synchrotron white beam X-ray topography (SWBXT)

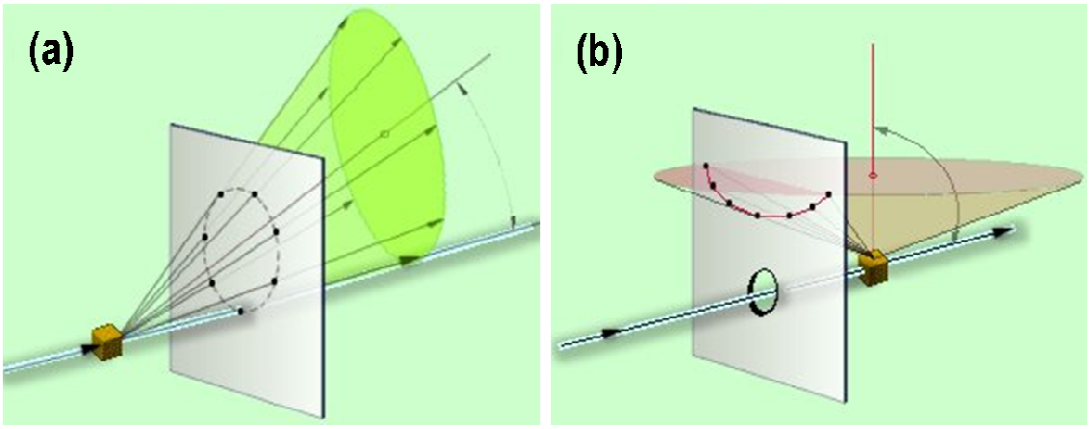

Figure 2.1 Schematic of Laue diffraction (a) Transmission method and (b) back-reflection method.[53]

Laue technique is used in this work to determine the orientation of LAST-18 single crystal samples. A beam of white radiation from a tube or a synchrotron is directed through a single crystal. Each set of planes in the crystal of a given interplanar spacing chooses its own λ from the beam such that the Bragg law is satisfied. The diffracted beams recorded on a photographic detector form an array of spots, which is called Laue diffraction pattern and can be analyzed to get the crystal

orientation.[54] There are two practical variants of Laue diffraction technique: the transmission method and the back-reflection method. Schematics of the two methods are shown in **Figure 2.1a** and **Figure 2.1b**, respectively.[53] In the transmission method, the film is placed behind the crystal to record beams that are transmitted through the crystal. In back-reflection method, a film is placed between the X-ray source and the crystal. The beams, which are diffracted in a backward direction, are recorded.

In this dissertation work, back-reflection Laue diffraction method had been used to help us find low-index planes of LAST-18 single crystals. In the molecular formula of LAST-18 or $AgPb_{18}SbTe_{20}$, heavy element Pb exists at a high percentage (57.3 wt.%), which absorbs most X-ray beams. As a result, we could not get diffraction patterns with sufficient information from regular tube-based X-ray sources, such as the Rigaku rotating anode X-ray generator at the Condensed Matter Physics and Materials Science Department of Brookhaven National Laboratory (BNL) and the Philips X-ray generator at Materials Science and Engineering Department of Stony Brook University. Compared with the conventional X-ray diffractometry, synchrotron white beam X-ray topography (SWBXT) has the advantage of high intensity, high spatial resolution, and broad spectral range. It is a powerful non-destructive tool to investigate the crystallographic orientations of various kinds of materials. When employing the synchrotron X-ray beam, it was still hard to get a reasonable transmission Laue pattern. Useful Laue patterns were finally obtained from the back-reflection method by using a long collection time. The SWBXT experiments were conducted at beam station X19C of the National Synchrotron Light Source

(NSLS) at BNL, which enable us to find desirable crystallographic orientations of the LAST-18 single crystals for further detailed TEM microstructure investigation.

2.2 X-ray powder diffraction (XRD)

X-ray powder diffraction (XRD) is a rapid analytical technique primarily used for phase identification of a crystalline material and can provide information on unit cell dimensions. There are several advantages in using XRD[55], which include: (1) It is a powerful and rapid technique for identification of an unknown mineral; (2) In most cases, it provides an unambiguous mineral determination; (3) Minimal sample preparation is required; (4) XRD instruments are widely available; (5) Data interpretation is relatively straightforward.

In this work, the phase compositions of melt-spun ribbons and sintered bulk samples of p-type filled skutterudite $CeFe_4Sb_{12}$ were examined by a Philips XRG 3100 X-ray diffractometer using Cu $K\alpha$ radiation (λ = 0.15418 nm). The average grain size of the melt-spun ribbons is estimated by using Scherrer's equation[56-57]

$$D = \frac{0.9\lambda}{B\cos\theta} \qquad (2.1)$$

where D is the grain size, λ is the X-ray wavelength, B is the full-width at half-maximum of the reflection peaks and θ is the diffraction angle. Instrumental broadening of the reflection peaks was obtained by using single crystalline silicon as the standard sample.

2.3 Optical microscopy

The optical microscope is the most convenient and inexpensive tool for the

microstructural characterization in materials science. Most materials are observed by reflection microscopy. The contrast mainly depends on local differences in the absorption and scattering of the incident light. With limited depth of field, opaque materials must be polished optically flat to be sharply focused at the best resolution.

In this work, a Nikon MM-40 optical microscope is used to observe the overall features of the fine polished random surface of the non-equilibrium synthesized and conventionally synthesized $CeFe_4Sb_{12}$ bulk samples. It is also used to check the thicknesses of the $CeFe_4Sb_{12}$ melt-spun ribbons.

2.4 Scanning electron microscopy (SEM)

Scanning electron microscopy (SEM) is one of the most versatile instruments for directly exploring microstructural features of solid objects.[58] It operates by scanning the sample surface with a high-energy beam of electrons in a raster scan pattern. Most commercial SEM instruments have the high spatial resolution on the order of 5 nm. Compared with an optical microscope, the large depth of field of an SEM enables it to image a specimen with big surface roughness. Additionally, SEM is also capable of examining a sample at very low magnifications to give overall microstructure information from a relatively large area of the sample.

A Hitachi S-4800 scanning electron microscope was utilized to characterize the surface morphology of the $CeFe_4Sb_{12}$ melt-spun ribbons and the fresh fracture surface morphology of the non-equilibrium synthesized and conventionally synthesized $CeFe_4Sb_{12}$ bulk samples.

2.5 Transmission electron microscopy (TEM)

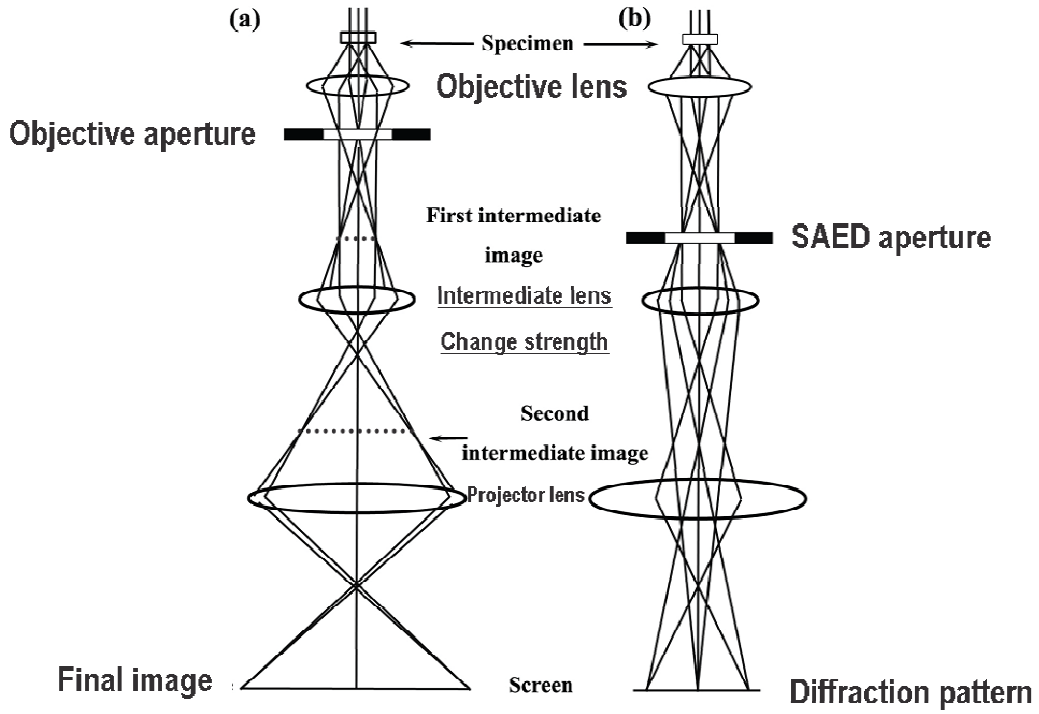

Figure 2.2 Ray diagrams of (a) imaging mode and (b) diffraction mode in TEM.

Transmission electron microscopy (TEM) is a microscopy technique whereby a beam of electrons is transmitted through an ultra thin specimen, interacting with the specimen as it passes through. Most important components in a transmission electron microscope are the illumination system and the imaging system. Ray diagrams of the imaging mode and diffraction mode of a three lens TEM microscope are shown in **Figure 2.2a** and **Figure 2.2b**, respectively. The beam of electrons from the electron gun is focused into a small, thin, coherent beam by the use of the condenser lens (not shown here), which excludes high angle electrons. The beam then hits on the specimen and part of it exits from the bottom surface of the specimen. The intermediate lens is normally focused on the intermediate image formed by the objective lens. Optional objective apertures can be used to enhance the contrast by blocking out high-angle diffracted electrons. When the intermediate lens is weakened

to focus on the back focal plane of the objective lens, the final image is an enlarged diffraction pattern. The use of selected-area electron diffraction (SAED) apertures ensures that only electrons coming from a chosen region in the specimen contribute to the diffraction pattern.

There are three types of image contrast in the TEM, which are the absorption contrast (sometimes called mass-thickness contrast), diffraction contrast and phase contrast. At low magnifications, TEM image contrast is due to the absorption of electrons in the sample, which is determined by the sample thickness and composition of the material. Diffraction contrast is simply a function of the diffraction conditions. It is a dominant mechanism for imaging dislocations and other defects in the specimen. However, the resolution of this imaging technique is limited to 1-3 nm. Diffraction contrast mainly reflects the long-range strain field in the specimen and it is unable, however, to provide high-resolution information about atomic distribution in the specimen.

Unlike the absorption and diffraction contrast mechanisms, which rely on the amplitude of scattered waves, phase contrast results whenever electrons of a different phase pass through the objective aperture. Contrarily to the TEM imaging at low and middle magnifications, HRTEM imaging does not rely on amplitudes, i.e. absorption by the sample, for image formation. Contrast in an HRTEM image is generated by measuring the amplitude resulting from this interference. However, the sample needs to be thin enough so that amplitude variations only slightly affect the image.

In this work, TEM has been used as the most important and powerful tool for the characterization of nanostructures in the material systems we studied. It is capable of directly imaging nanostructures and defects at the level of atomic resolution.

Electron diffraction provides an easy way to get the local crystallographic information of nanostructures and matrix in a material. In addition, TEM is easy to be combined with other various detectors to supply multiple information of the material. For example, a TEM equipped with energy dispersive X-ray spectrometry (EDS) detector allows the acquisition of qualitative and semi-quantitative chemical compositional information in a sample.

TEM instruments widely used in this work include JEOL JEM 2100F, 3000F, and 2200MCO at BNL. JEM-2100F[59] is equipped with a schottky field-emission gun and two exchangeable objective-lens pole-pieces. The ultra high resolution pole piece has a 0.19 nm point-to-point resolution and a ±20° sample tilt, and the high resolution pole piece has a 0.23 nm point-to-point resolution and a ± 40° sample tilt. It is also equipped with an Oxford energy dispersive X-ray spectrometer for chemical analysis, and heating and cooling stages for in-situ experiments and dynamic observations. JEM-3000F is equipped with an ultra high resolution objective-lens pole piece, an off-axis 1024×1024 Gatan slow-scan camera, a Fischione annular dark field detector, a post column Gatan imaging filter, and a Noran X-ray detector. JEOL JEM-2200MCO is used for imaging the ultra-small nanoprecipitates in the LAST-18 single crystals. It is equipped with two spherical aberration (Cs) correctors with one for condenser lens and the other one for objective lens. With the dual Cs-correctors, the microscope has the ability to achieve sub-angstrom resolution in both TEM and STEM modes.

In this work, size, shape, distribution of nanostructures and defects of the LAST-18 single crystals and $CeFe_4Sb_{12}$ melt-spun ribbons and sintered bulk samples were observed by bright-field TEM and HRTEM imaging. Selected area electron

diffraction (SAED) patterns and fast Fourier transform (FFT) diffractograms help to figure out lattice symmetries of nanoprecipitates and other defects, as well as their orientation relationships with the matrix. Accurate lattice parameters, lattice mismatch and average strain have been measured by fitting the line scan of density profiles from the central spot to reflection spots in the SAED pattern or FFT diffractograms with a combined Gaussian and Lorentzian function

$$I = a_0 \exp\left[-\left(\frac{x-a_1}{a_2/(2\ln 2)}\right)^2\right] + \frac{a_3}{4(x-a_1)^2 + a_2^2} + a_4 \qquad (2.2)$$

where, a_0 and a_3 are the amplitudes of the Gaussian and Lorentzian function, respectively, a_1 is the position of the peak, a_2 is the full width at half maximum (FWHM) height of the peak, a_4 is the base line offset. Chemical composition information of nanostructures was obtained by using EDS analysis. Due to the errors caused by the small size of the nanoprecipitates, the composition information obtained by EDS is taken as semi-quantitatively.

2.6 Geometric phase analysis (GPA) software

Through the measurements of the lattice mismatches between the nanoprecipitates and the surrounding matrix lattices, average strains caused by the nanoprecipitates were easily obtained. The local distribution of the strain fields around nanoprecipitates in LAST-18 single crystals and $CeFe_4Sb_{12}$ polycrystals were retrieved using geometric phase analysis (GPA) software. GPA is a commercial software for generating fully quantitative deformation and strain maps from standard

HREM images based on the geometric phase algorithms originally developed by Martin Hytch.[60-62]

The first step is to calculate the power spectrum which is the Fourier transform of the HRTEM image. Phase image is obtained by centering a small aperture on a strong reflection spot g in the power spectrum, followed by an inverse Fourier transform.[63] The phase component $P'_g(r)$ of the phase image is related to the lattice displacement $u(r)$ by

$$P_g(r) = P'_g(r) - 2\pi g_0 \cdot r = -2\pi g \cdot u(r) \tag{2.2}$$

where g_0 is the reciprocal lattice vector from the undistorted reference lattice.

The two-dimensional displacement field can be derived by applying the method to two non-collinear Fourier components, e.g. g_1 and g_2.

$$P_{g1}(r) = -2\pi g_1 \cdot u(r) = -2\pi[g_{1x}u_x(r) + g_{1y}u_y(r)] \tag{2.3}$$

$$P_{g2}(r) = -2\pi g_2 \cdot u(r) = -2\pi[g_{2x}u_x(r) + g_{2y}u_y(r)] \tag{2.4}$$

where g_{1x}, g_{1y}, g_{2x} and g_{2y} are the x and y components of the g_1 and g_2 vectors, respectively. $u_x(r)$ and $u_y(r)$ are the x and y components of the displacement field $u(r)$ at the position $r = (x, y)$ in the image. The strain field is then calculated by

$$\varepsilon_{xx} = \frac{\partial u_x}{\partial x}, \quad \varepsilon_{yy} = \frac{\partial u_y}{\partial y} \tag{2.5}$$

2.7 TEM sample preparation

TEM sample preparation is one of the most difficult parts in a TEM work. TEM samples need to be less than 100 nm, which is the thickness that electrons can pass through the sample. High quality TEM images can only be obtained from TEM samples with large thin areas with minimum contaminations and artifacts. It is generally accepted that TEM sample preparation takes more than 50% importance in a TEM work.

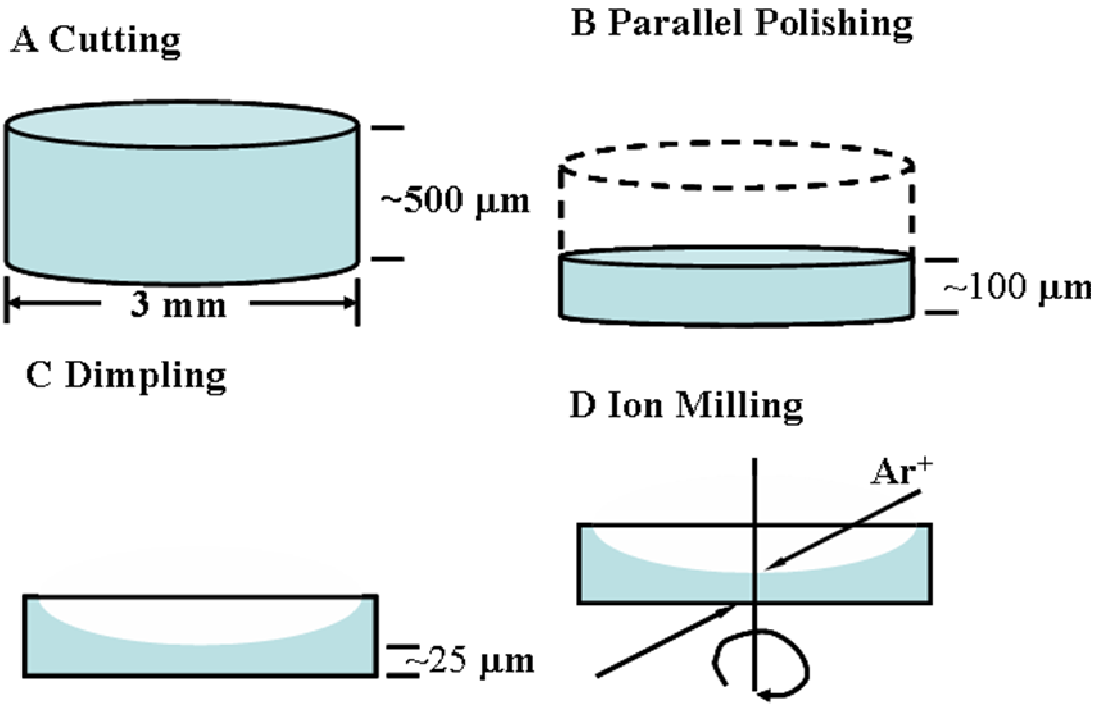

Figure 2.3 Schematic of traditional dimpling TEM sample preparation process.

LAST-18 single crystals and $CeFe_4Sb_{12}$ polycrystals TEM samples have been successfully prepared by the traditional dimpling method. A schematic of the TEM sample preparation process by this method is shown in **Figure 2.3a** to **Figure 2.3d**. The first step is to cut a 500 μm thick slab from ingot. The slab was cut into smaller rectangular pieces with longest side less than 2.5 mm using wire saw, or into disks with diameter of 3 mm using ultrasonic disk cutter. Either diamond or Al_2O_3 lapping

films were used for mechanical polishing of both kinds of samples. The sequence of diamond lapping films and wheel speed are 15 μm at 100 rpm, 3 μm at 70 rpm, 1 μm at 50 rpm, and 0.5 μm at 20 rpm. The small pieces or 3 mm disks are coarsely polished on one side and fine polished on the other side till a thickness about 100 μm using a disk grounder tool and the mechanical polisher. The fine polished side of sample is glued onto a copper grid with M-Bond 610 adhesive and the coarsely polished side is dimpled till the thickness near 25 μm. The final step is using ion miller to thin the sample to electron transparency thickness which is around or below 100 nm at low milling angles less than 12°. The specimen stage of the ion mill system can be cooled by liquid nitrogen, which helps avoid local specimen overheating during the milling process and eliminate the production of artifacts in the final sample. All of the LAST-18 single crystal and $CeFe_4Sb_{12}$ polycrystal TEM samples were ion milled below negative 90 ^{o}C.

TEM samples of melt-spun $CeFe_4Sb_{12}$ ribbons were prepared by grinding the brittle ribbons into very fine powders. A droplet of dilute solution of the fine powders in ethanol alcohol was placed onto a lacey film coated copper grid to dry.

3. TEM investigation of nanostructures and defects in LAST-18 single crystals

3.1 Introduction

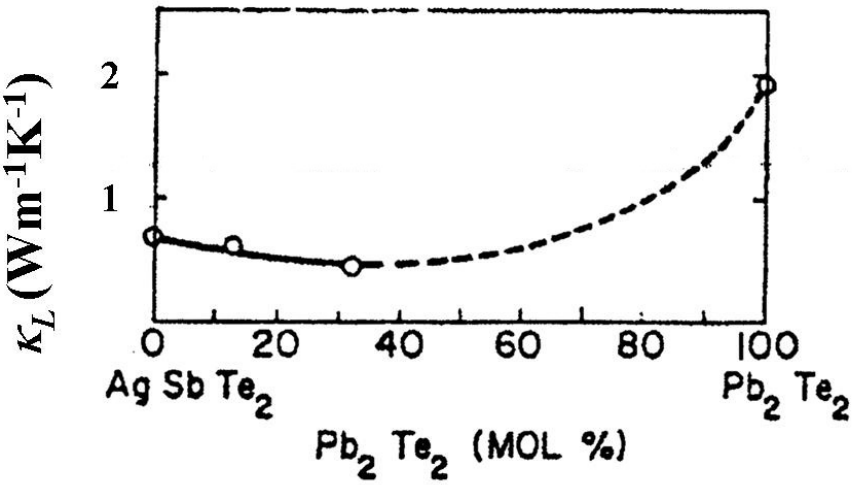

Figure 3.1 Variation of lattice thermal conductivity κ_L with composition in the $AgSbTe_2$-PbTe alloy system.[64]

The alloys of $AgSbTe_2$ and PbTe had been reported to form a solid solution with NaCl structure.[64] The variation of lattice thermal conductivity κ_L with composition in the system is shown in **Figure 3.1**. The minimum κ_L is 0.45 $Wm^{-1}K^{-1}$ at the composition of 50%$AgSbTe_2$-50%PbTe. However, the electrical resistivities of $AgSbTe_2$-PbTe alloys were found to be relatively high (on the order of 10^{-4} Ω·m) (**Figure 3.1**), which resulted in low *ZT* values.

Table 3.1 Electrical resistivity and Seebeck coefficient of $AgSbTe_2$-PbTe alloys at 300 K.[64]

Alloy Composition	ρ (Ω·m)	S (μVK^{-1})
75%$AgSbTe_2$ - 25%PbTe	3.1×10^{-4}	300
50%$AgSbTe_2$ - 50%PbTe	5.0×10^{-4}	350
40%$AgSbTe_2$ - 60%PbTe	3.0×10^{-4}	380

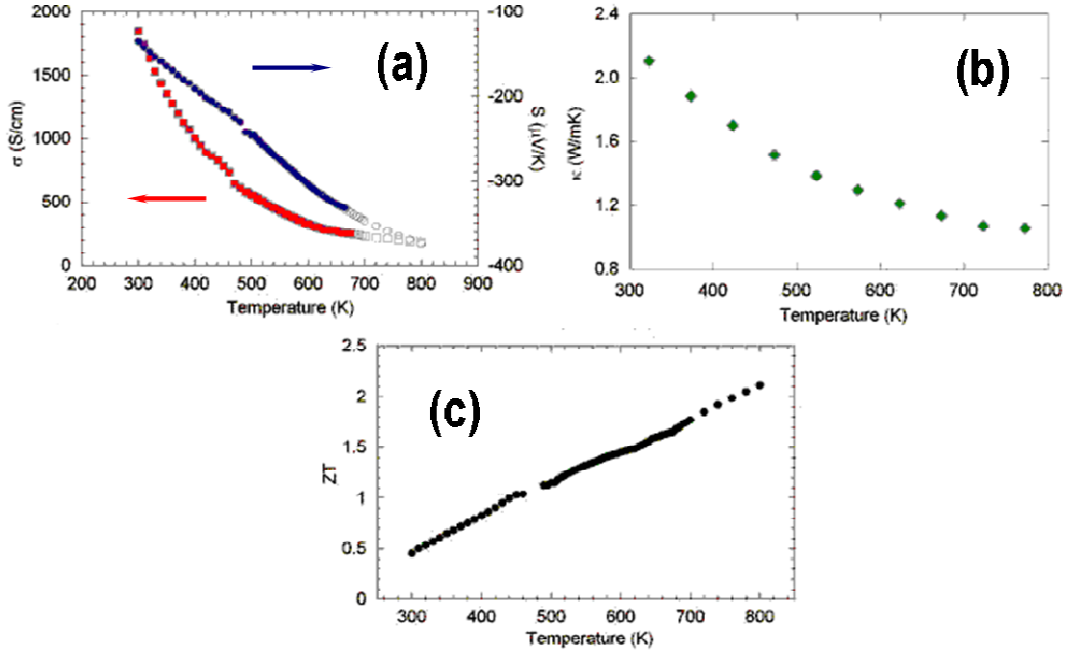

Figure 3.2 Temperature dependence of (a) Electrical conductivity σ (red line) & Seebeck coefficient S (blue line); (b) thermal conductivity κ; (c) figure of merit ZT of LAST-18.[28]

Enhancement by increasing electrical conductivity without much loss in Seebeck coefficient was obtained in the LAST-m compounds which have compositions deviating from the ideal stoichiometry.[28] As shown in **Figure 3.2a**, the LAST-18 ($AgPb_{18}SbTe_{20}$ or $(PbTe)_{1-x}(AgSbTe_2)_x$ with x ~ 0.05) sample shows a very low electrical resistivity of $\rho \approx 5.4\times10^{-6}$ Ω·m at room temperature, which is about 2 orders of magnitude lower than the $AgSbTe_2$ and PbTe alloys as shown in **Table 3.1**. Absolute value of the Seebeck coefficient S increases with increasing temperature, reaching 370 μVK^{-1} at 800 K. The total κ is measured to be 2.3 $Wm^{-1}K^{-1}$ at room

temperature and keeps decreasing to 1 $Wm^{-1}K^{-1}$ at 800 K (**Figure 3.2b**). The lattice thermal conductivity κ_L is calculated to be 0.65 $Wm^{-1}K^{-1}$ at 800 K by using the Wiedemann-Franz law, which is close to the minimum value obtained from $AgSbTe_2$-PbTe alloys. The *ZT* value is 1.7 at 700 K and extrapolated to 2.1 at 800 K.

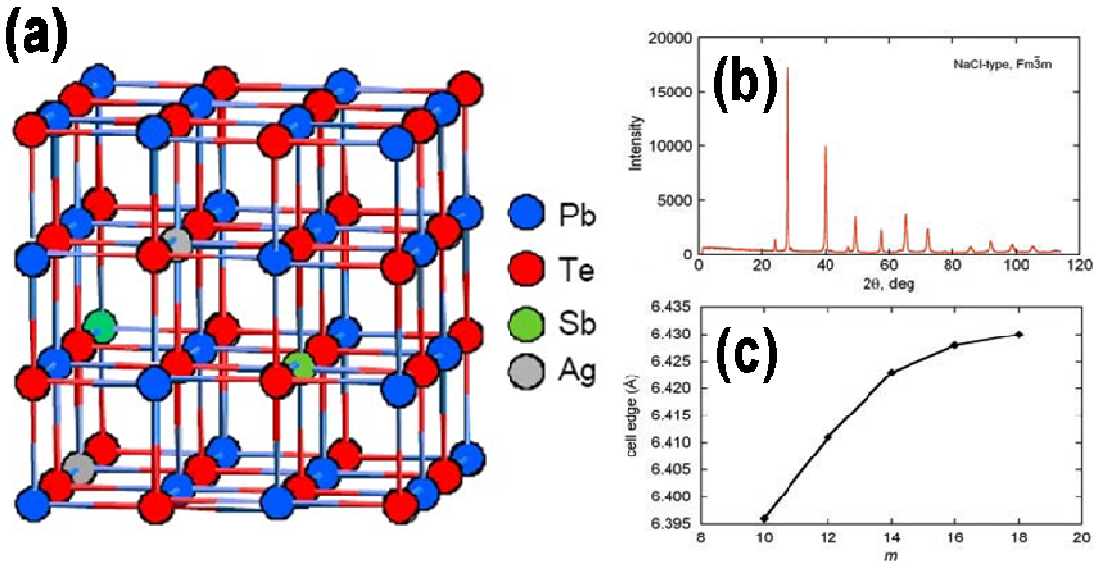

Figure 3.3 (a) Average Fm3m crystal structure of LAST-m compounds; (b) X-ray diffraction pattern of $AgPb_{10}SbTe_{12}$; (c) Variation of unit cell parameter as a function of m of $AgPb_mSbTe_{m+2}$ (LAST-m) compounds.[65]

LAST-m compounds are generally believed to possess an average NaCl structure (Fm3m symmetry), in which Te atoms occupy the Cl sites, while Pb, Ag and Sb atoms are disordered on the Na sites (**Figure 3.3a**).[64] The X-ray powder diffraction pattern of $(PbTe)_{10}(AgSbTe_2)_1$ (LAST-10) in **Figure 3.3b** shows single phase crystallizing in a face-centered cubic (FCC) structure. The variation of unit cell parameters with *m* roughly obeys Vegard's law (**Figure 3.3c**).[65] These are the supporting evidences that LAST-m compounds form solid solutions between $AgSbTe_2$ and PbTe.

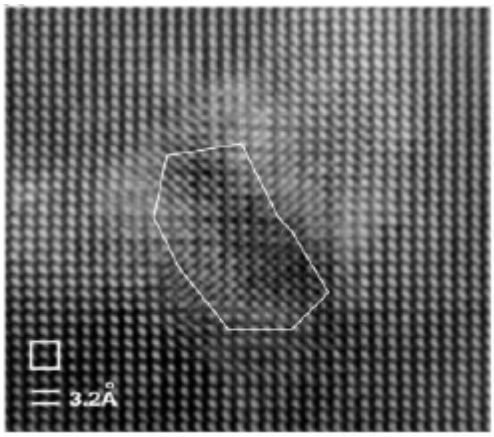

Figure 3.4 HRTEM image of a $(PbTe)_{18}(AgSbTe_2)_1$ sample showing a "nano-dot" in the enclosed region.[28]

However, further single crystal X-ray diffraction and electron diffraction studies reveal that Ag and Sb atoms are not randomly disordered with Pb atoms and thus LAST-m compounds are not simple solid solutions between $AgSbTe_2$ and PbTe phases.[65] The homogeneous compounds of this system have been synthesized by the quenching method; however, these quenched samples exhibit much inferior thermoelectric properties.[66] High resolution TEM (HRTEM) image in **Figure 3.4** demonstrates a nanometer scale inclusion of Ag-Sb rich phase embedded in the PbTe matrix in a LAST-18 sample.[28, 65] This indicates LAST-m compounds are actually host materials containing nanostructures.

Ab initio electronic calculations based on different Ag-Sb arrangements reveal that the electronic structure and consequently, the electronic and thermal transport properties of LAST-m compounds, are different from those of PbTe and very sensitive to the atomistic arrangements of Ag-Sb atoms.[67] The electronic structure calculations by D. I. Bilc *et al.* in 2004 have revealed an enhanced density of states

near the band gap in LAST-m systems, which was suggested to be able to enhance power factors.[67] Their further transport calculations in 2006 revealed that the enhancement of the density of states could give rise to only a small increase in power factor. The strong reduction in κ_L caused by the presence of nanoprecipitates and other defects played a key role for the remarkable *ZT* enhancements in the LAST-18 samples.[68]

A variety of other thermoelectric materials with improved thermoelectric properties have also been reported to have similar nanostructures embedded in matrix lattices.[69-70] In order to understand the role of nanostructures on thermoelectric properties, comprehensive structural characterization of the nanostructures is needed. The nanoprecipitates in LAST-m compounds involve clustering and ordering of Ag, Sb, and Pb atoms. However, detailed structural information such as size, shape, distribution, orientation, lattice parameters, strain fields, defects, and ordering of Ag-Sb with Pb atoms of the nanoprecipitates, which substantially influence thermoelectric properties of a material, is still lacking.

Consequently, the motivation of this part of work is to carry out an extensive structural investigation of nanoprecipitates and other defects in LAST-18 single crystals by using TEM/HRTEM techniques. We hope such information will be useful for more realistic theoretical modeling and leads to better fundamental understanding of this class of materials.

3.2 Materials synthesis

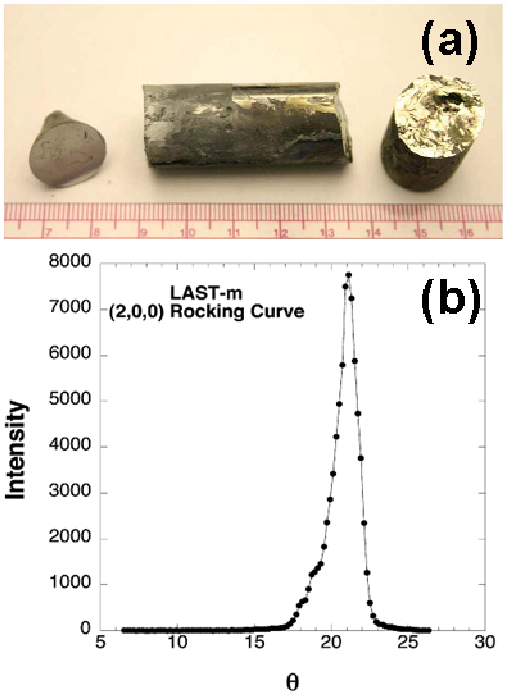

Figure 3.5 (a) A typical LAST-18 single crystal grown by the Bridgman method at General Motors R&D Center; (b) (200) rocking curve of a LAST-18 single crystal from neutron diffraction.

In this work, LAST-18 single crystals were supplied by our collaborators Dr. Jihui Yang and his colleagues at General Motors R&D Center. One of the typical LAST-18 single crystal ingots is shown in **Figure 3.5a**. Stoichiometric amounts of high purity Ag, Sb, Pb and Te pieces were loaded into a carbon-coated quartz tube. The tube was sealed under vacuum and slowly heated up to 1000 °C. It was then held at this temperature for 20 hours to make sure the melt was completely homogeneous. After this, the tube was cooled down to room temperature by turning the power off. The resulting ingot was then solidified by the Bridgman method inside a 4-zone furnace. It was heated up to 950 °C (about 40 °C above the liquidus) and held for 3 hours, then soaked at the liquidus of 910 °C for 61 hours. When the crystal started to

grow, the furnace translation rate was increased to 1 mm per hour. After a total translation of 25.5 mm, the translation stopped and the furnace was cooled down by turning the power off. Corresponding rocking curve from neutron diffraction of this crystal is shown in **Figure 3.5b**. The Bragg peak along the (200) direction has a full-width-at-half-maximum (FWHM) of 1 ~ 2 º, which indicates the single crystal of high quality.

3.3 Results and discussion

3.3.1 Overview of the LAST-18 single crystal samples

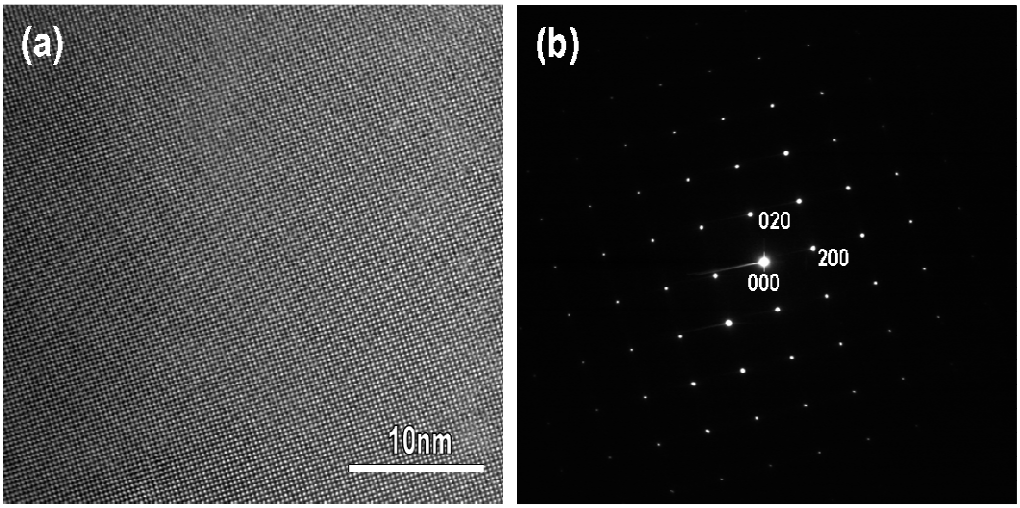

Figure 3.6 (a) HRTEM image and (b) Electron diffraction pattern of a LAST-18 single crystal sample.

An HRTEM image of the matrix of a LAST-18 single crystal sample is shown in **Figure 3.6a**. Electron diffraction analysis by tilting the sample to several low-index zones confirms that the matrix has the face-centered cubic (FCC) rock-salt type structure with space group Fm3m. One of the electron diffraction patterns with the

zone axis along [001] direction is shown in **Figure 3.6b**. The lattice parameter of the matrix varies locally from 0.625 nm to 0.660 nm.

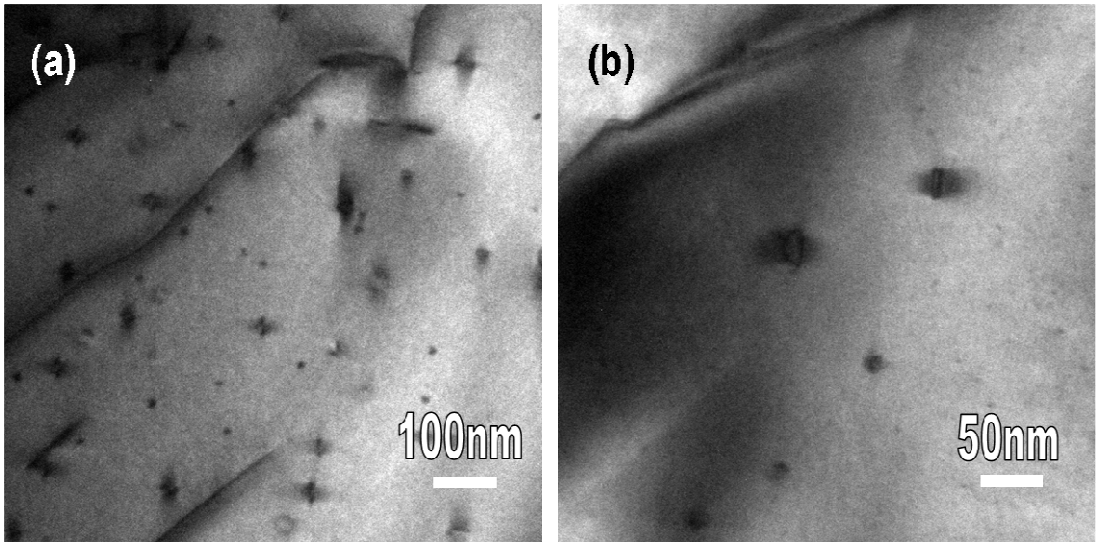

Figure 3.7 (a) Low magnification TEM image showing nanoprecipitates with varying size and shape in a LAST-18 single crystal sample; (b) TEM image showing the existence of strain field around the nanoprecipitates.

Extensive TEM observations revealed that dominant microstructural defects in the LAST-18 single crystals include dislocations, strain fields and most distinctly, a widespread existence of nanoprecipitates. **Figure 3.7a** is a low magnification TEM image showing the nanometer scale precipitates with varying sizes and shapes embedded in the matrix of a LAST-18 single crystal sample, as well as the contrast caused by the low angle grain boundaries. The TEM image at a higher magnification in **Figure 3.7b** demonstrates more clearly the existence of strain fields around the nanoprecipitates.

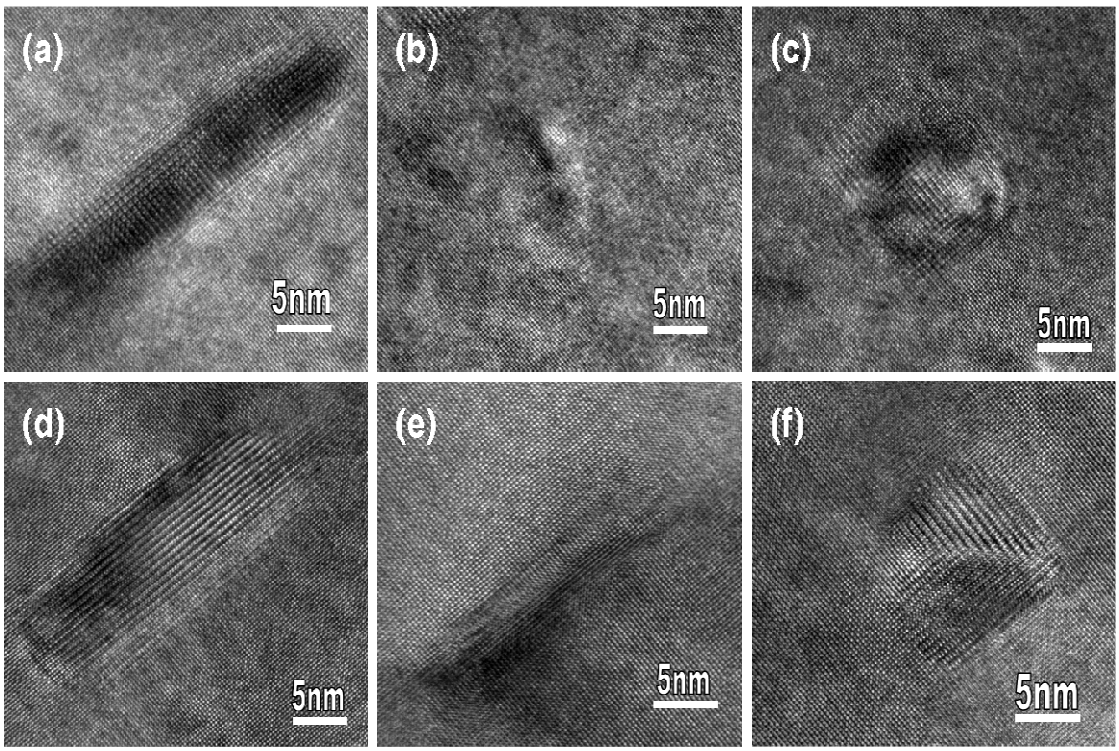

Figure 3.8 (a - f) HRTEM images showing several nanoprecipitates present in LAST-18 single crystal samples with different size and shape.

HRTEM observations show that nanoprecipitates in LAST-18 single crystals have different shapes such as cubic, rectangular, butterfly-like, elliptical and other irregular shapes. Several typical ones of them are shown in **Figure 3.8**. Most of them have sizes from several few nanometers to about 20-30 nm.

Comprehensive TEM imaging and EDS chemical analysis of nanoprecipitates show that they possess varying chemical compositions, crystal symmetries, lattice mismatch and strain fields with surrounding matrix.[63] Detailed structure analysis of nanoprecipitates was conducted by using the WImage software developed by Dr. Lijun Wu at BNL. In the next three sections, several nanoprecipitates are taken as examples to show our detailed microstructure analysis process of nanoprecipitates.

3.3.2 Nanoprecipitates with primitive cubic structure

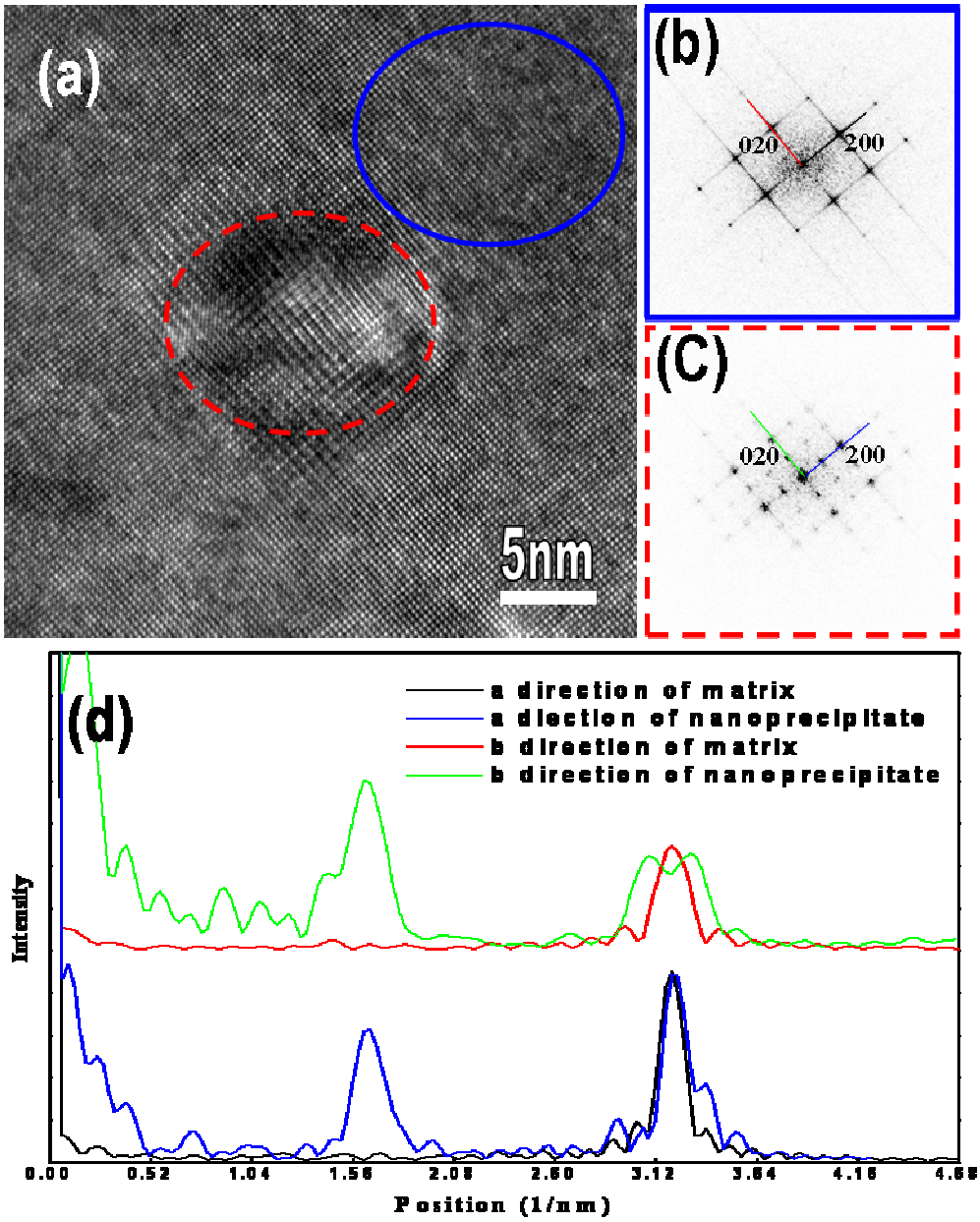

Figure 3.9 (a) HRTEM image showing a nanoprecipitate in a LAST-18 single crystal sample; (b-c) Diffractograms from the elliptical matrix and nanoprecipitate areas highlighted in (a), respectively; (d) Line scans from central spot 000 to 200 and 020 spots of the diffractograms.

Figure 3.9a is an HRTEM image of a LAST-18 single crystal sample which shows a square shaped nanoprecipitate coherently embedded in the matrix. To

accurately measure the lattice parameters, the elliptical areas marked by the solid blue line in matrix and dashed red line in nanoprecipitate in **Figure 3.9a** are selected and conducted fast Fourier transform (FFT) to get diffractograms of the images. **Figure 3.9b** and **Figure 3.9c** are the corresponding FFT diffractograms of the marked matrix and nanoprecipitate areas in **Figure 3.9a**. From **Figure 3.9b**, the matrix is confirmed to be in the FCC structure, in which [100] and [010] reflections are invisible due to the extinction of FCC structure when *h, k, l* having mixed parity. However, [100] and [010] reflections are present in the diffractogram of the nanoprecipitate in **Figure 3.9c**, indicating that the structure of the nanoprecipitate is different from that of the matrix. The nanoprecipitate is indexed to be a primitive cubic (Pm3m) structure.

A profile from the central spot to the reflection spot is obtained for the measurement and comparison of the reflection spots in the diffractograms of different areas. The black and red lines in **Figure 3.9d** are the 200 and 002 line scans from diffractogram of the matrix (**Figure 3.9b**), respectively. The blue and green lines are the 200 and 020 line scans from the diffractogram of the nanoprecipitate (**Figure 3.9c**), respectively. The accurate lattice parameters were obtained by fitting the profile using the combined Gaussian and Lorentzian function. The lattice parameter *a* of the matrix and nanoprecipitate is determined to be 0.625 nm and 0.621 nm ($a_{nano} \approx a_{matrix}$), respectively. The lattice parameter *b* of the matrix is refined to be 0.624 nm. The green profile from the 020 line scan of the nanoprecipitate shows splitting of 020 peaks with one at 3.078 nm^{-1} and the other at 3.30 nm^{-1}. This implies that the nanoprecipitate consists of two parts, one has lattice parameter b = 0.650 nm, while

the other has b = 0.606 nm. They are 4% larger and 3% smaller than the matrix lattice parameter of a = 0.625 nm measured along the [010] direction, respectively. We noticed that there is slight difference between the lattice parameters of a and b of the nanoprecipitate. We consider this is caused by the strain around the nanoprecipitate.

Similar analysis at several different locations containing nanoprecipitates with Pm3m lattice in LAST-18 single crystal samples shows that they have different lattice mismatch with the FCC matrix. The biggest mismatch we observed is approximately 6% along the [100] direction.

3.3.3 Nanoprecipitates with primitive tetragonal structure

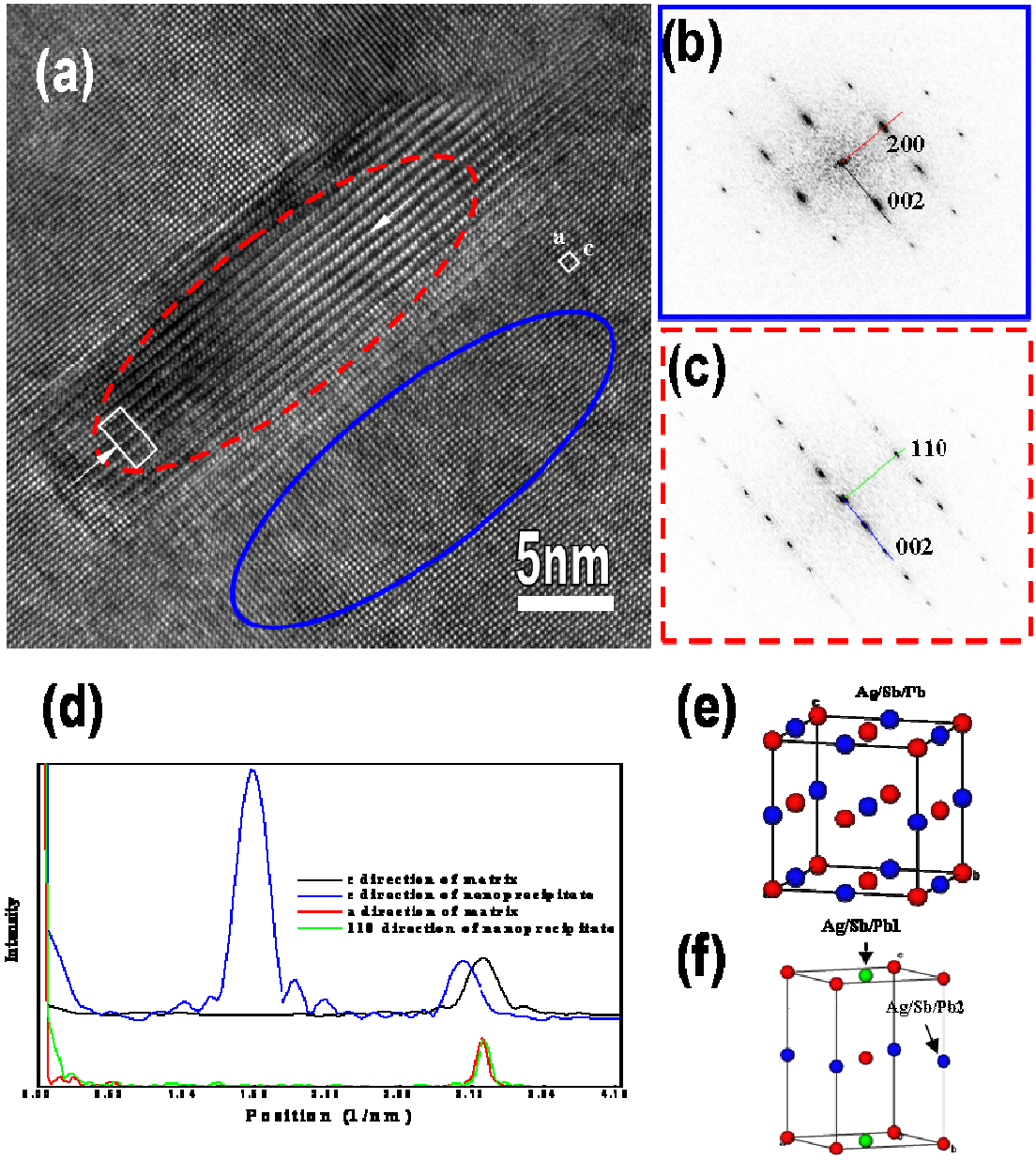

Figure 3.10 (a) HRTEM image of a LAST-18 single crystal sample, showing a nanoprecipitate coherently embedded in the matrix; (b) Diffractogram from the ellipse matrix area; (c) Diffractogram from the ellipse nanoprecipitate area; (d) Line scans from central spot 000 to 002 and 200/110 spots of the diffractograms; (e) Atomic models of the matrix; (f) Atomic models of the nanoparticle. The atomic ratio of Pb:Sb:Ag of Pb/Sb/Ag1 site is different from that of Pb/Sb/Ag2 site. The HRTEM simulation (from Dr. Lijun Wu) is carried out based on the structure model with pure Pb in Pb/Sb/Ag1 and Pb:Sb:Ag = 50:25:25 in Pb/Sb/Ag2. The simulation is shown in the inset of (a), which is in good agreement with the experiment.

We also observed nanoprecipitates with primitive tetragonal lattice symmetry. **Figure 3.10a** is an HRTEM image of a LAST-18 single crystal sample which shows a rectangular nanoprecipitate in the matrix. The unit cell is marked by a white square in which there are two atomic planes showing the same contrast. While within the nanoprecipitate, the (001) atomic planes of the nanoprecipitate at $c = 0$ and $c = 1/2$ position show different contrast, indicating the ordering along the [001] direction. The contrast of the two atomic planes marked by the white arrow lines in the nanoprecipitate reverses or shifts one atomic layer along [001] direction with each other, which indicates the existence of anti-phase boundaries. Comparing to the structure of the matrix which has FCC lattice (**Figure 3.10e)**, the Ag/Sb/Pb sites in the nanoprecipitate are not equivalent to each other due to different Ag:Sb:Pb ratios (**Figure 3.10f)**. Apparently, the exchange of Ag/Sb/Pb ratios, or equivalently ½[111] shifting of the unit cell yields anti-phase domains and the contrast along [001] direction. We also observed the existence of many dislocations in the nanoprecipitate, as one of them labeled with the white dislocation sign. The increased interface due to the anti-phase boundaries and dislocations would enhance phonon scattering, thus further reduce the thermal conductivity.

FFT diffractograms of the marked areas in the matrix and the nanoprecipitate in **Figure 3.10a** are shown in **Figure 3.10b** and **Figure 3.10c**, respectively. The matrix is still determined to be the FCC structure, while the nanoprecipitate is indexed to be the primitive tetragonal (P4/mmm) in symmetry.

A profile from the central spot to the reflection spot is then obtained for the measurement and comparison of the reflection spots from different areas. The black and red lines in **Figure 3.10d** are the 002 and 200 line scans from the diffractogram of the matrix in **Figure 3.10b** and the blue and green lines are the 002 and 110 line scans from the diffractogram of nanoprecipitate in **Figure 3.10c**, respectively. It is shown that the 002 peak from the nanoprecipitate shifts to the left and gets closer to the central spot than that from the matrix, indicating that the lattice parameter *c* of the nanoprecipitate is larger than that of the matrix. The lattice parameters *c* of the matrix and nanoprecipitate obtained by Gaussian and Lorentzian fitting the profiles are 0.626 nm and 0.654 nm, respectively. The lattice parameter *c* of the nanoprecipitate is 4.5% larger than that of the matrix. The lattice parameter *a* of the matrix and the nanoprecipitate is determined to be 0.627 nm and 0.441 nm ($a_{matrix} = \sqrt{2}\, a_{nano}$). The lattice change of the nanoprecipitate mainly occurs along [001] which is the ordering direction of the nanoprecipitate.

Figure 3.10e and **Figure 3.10f** show the structure models provided by Dr. Lijun Wu of the matrix and the nanoprecipitate, respectively. Compared to the structure of the matrix which has FCC lattice, Pb and Pb/Ag/Sb atoms order along the c direction in the nanoprecipitate. Apparently, the exchange of Pb and Pb/Ag/Sb, or equivalently ½[111] shifting of the unit cell yields the anti-phase domain.

EDS measurements showed that the composition of the nanoprecipitate is slightly Ag-Sb rich than the matrix area. The HRTEM simulation in the marked white

rectangular area in **Figure 3.10a**, based on the structure model with Pb:Ag:Sb = 50:25:25 at Pb/Ag/Sb site, shows good agreement with the experiment.

Besides the primitive cubic and primitive tetragonal structures, nanoprecipitates with body centered tetragonal lattices with doubled or tripled lattice parameters along the *c* direction have also been observed in the LAST-18 single crystal samples. Detailed description about the structural analysis of these nanoprecipitates can be found in our published paper.[63]

3.3.4 Strain fields associated with nanoprecipitates

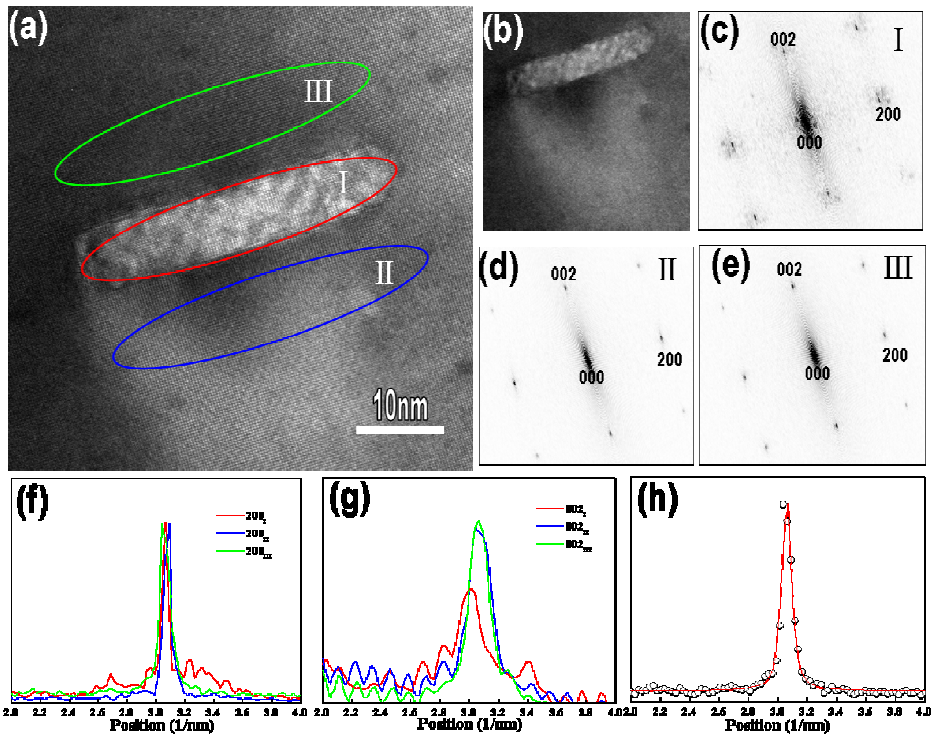

Figure 3.11 (a) HRTEM image of an elliptical nanoprecipitate in the LAST-18 single crystal; (b) Low-magnification image of the nanoprecipitate in (a), showing strain-field contrast; (c-e) Diffractograms from the elliptical area I (c), II (d), and III (e), respectively; (f-g) 200 and 002 intensity profiles from the diffractograms (c), (d), and (e), respectively; (h) Combined Gaussian and Lorentizian fit (red line) to 200 reflection of the matrix area III (open circles).

Strain contrast has been observed around most of the nanoprecipitates in LAST-18 single crystals. An example is given in **Figure 3.11a** and **Figure 3.11b**. The diffractograms of the nanoprecipitate area I and the matrix area II (with strain contrast) and III (without strain contrast) are shown in **Figure 3.11c**, **Figure 3.11d**, and **Figure 3.11e**, respectively. Weak 001 and 100 reflection spots are present in the diffractogram of the nanoprecipitate area I (**Figure 3.11c**), indicating that the nanoprecipitate has a primitive tetragonal lattice. The intensity profiles of the 200 reflections of the diffractograms in **Figure 3.11c**, **Figure 3.11d** and **Figure 3.11e** are shown in **Figure 3.11f**, from which we can see the positions of 200 peaks of area I, II, and III are quite close to each other. The lattice parameters along the [100] direction are obtained by fitting these profiles using a combined Gaussian and Lorentzian function to be a_I = 0.653 ± 0.002 nm, a_{II} = 0.650 ± 0.002 nm and a_{III} = 0.654 ± 0.002 nm, respectively. The difference is within the measurement error. The intensity profiles of the 002 reflection peaks are shown in **Figure 3.11g**. The 002 peak profile of area I (red line**)** is much broader than those of area II and III. It splits into two peaks with one at 3.005 ± 0.038 nm^{-1} and the other at 3.407 ± 0.043 nm^{-1} in position. This indicates that the nanoprecipitate has two phases, one with c = 0.660 ± 0.005 nm, while the other with c = 0.587 ± 0.003 nm. The lattice parameters of the matrix area II and III are determined to be equal to each other with c = 0.652 ± 0.002 nm.

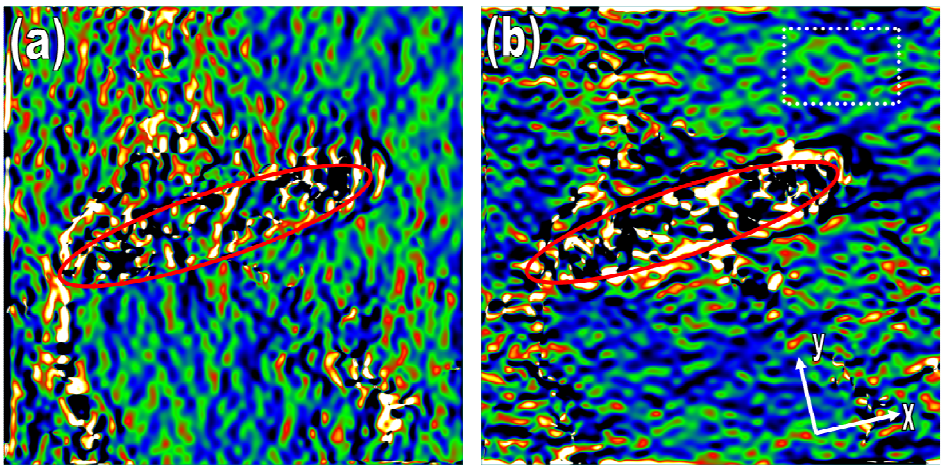

Figure 3.12 Strain-field of (a) ε_{xx} and (b) ε_{yy} calculated from the HRTEM image shown in Figure 3.11a. The white dotted rectangle in (b) is the reference area which has an average strain of -0.02. The images are shown in color for clarity. The ellipses in the figures outline the nanoprecipitate area.

The distribution of the strain-field can be retrieved using the GPA software. The strain map derived by GPA software is relative to the reference area. The average strain in the reference area can be calculated by measuring the average lattice parameter in the area. The actual strain-field map is thus the sum of the average strain of the reference area and the relative strain obtained from GPA software. The actual strain maps of ε_{xx} and ε_{yy} are shown in **Figure 3.12a** and **Figure 3.12b**, respectively, which were retrieved from **Figure 3.12a** with *x* and *y* axis pointing to the [100] and [001] direction. The reference area marked by a white dotted rectangle in **Figure 3.12b** was measured to have an average strain value of -0.02 in both directions with respect to the undistorted area. The ε_{xx} and ε_{yy} maps show both positive and negative strain in the nanoprecipitate area, indicating a phase separation in this area, consistent with the lattice measurement from diffractograms. The low magnification TEM image (**Figure 3.12b**) shows that the strain contrast extends to about 50 nm away from the

nanoprecipitate. The strain in the matrix is quite different from that generated by an isotropic misfitting spherical inclusion in an infinite isotropic matrix. The ε_{xx} and ε_{yy} strain around nanoprecipitate is not symmetric. Close to the nanoprecipitate area, the ε_{xx} and ε_{yy} maps show dominantly positive strain on top of the nanoprecipitate and negative strain below it. The strain-field around the nanoparticle may be caused not only by the misfit between the nanoparticle and the matrix, but also by the local fluctuation in the composition. When nanoprecipitates are formed, they consume Ag-Sb, resulting in the compositional fluctuations in the surrounding matrix.

3.3.5 Atomistic arrangements and nucleation of nanoprecipitates

The remarkable enhancement of *ZT* of LAST-18 samples has been attributed to the large reduction in κ_L caused by the presence of nanoprecipitates. It has been suggested that the endotaxially-embedded nanoprecipitates in the matrix lattices provide highly conductive paths that allow carrier transport unaffected or much less affected. However, the high density of interfaces between nanoprecipitates and matrix will act as barriers for phonon propagation. In our study, nanoprecipitates with varying size, shape, and contrast have been observed by TEM and HRTEM imaging in the LAST-18 single crystals. Detailed structure analysis reveals that these nanoprecipitates possess different crystal symmetry, chemical composition, lattice mismatch, and strain field with the matrix lattice. Two important questions that may come up would be: (i) how are the nanoprecipitates formed, and (ii) how do they interact with the matrix lattice? Experimental work that can give a clear picture of the

atomic arrangements of the nanoprecipitates in this material system is not available. Without doubt, such a work will help clarify the underlying principle that controls the formation of nanoprecipitates and their interactions with the matrix lattice.

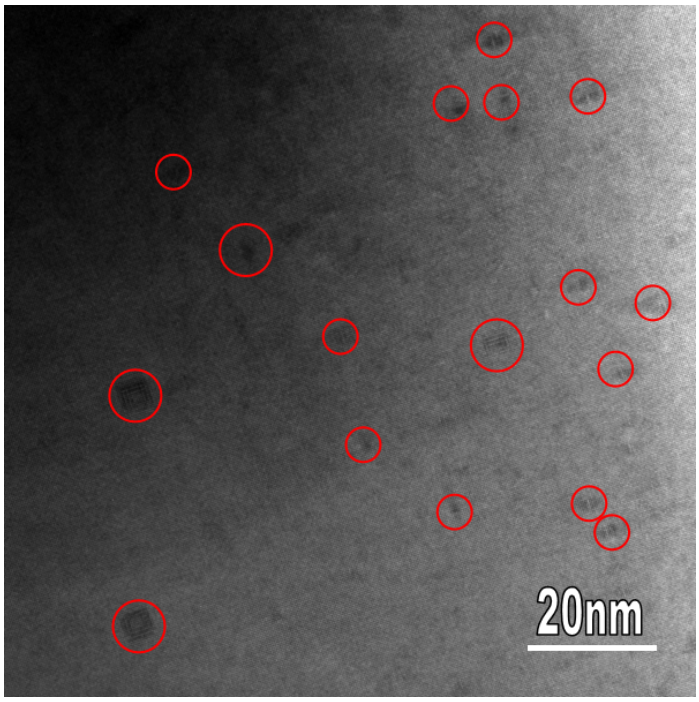

Figure 3.13 (a) A TEM image of a LAST-18 single crystal sample, showing the cube-like and plate-like nanoprecipitates highlighted by the big and small red spheres, respectively. They are found to exist ubiquitously in the sample.

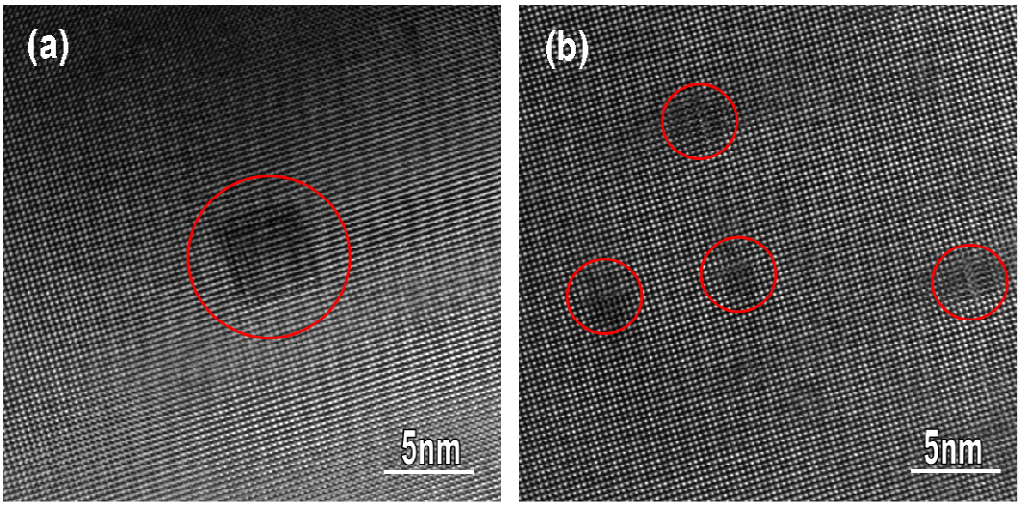

Figure 3.14 (a) and (b) HRTEM images of cube-like and plate-like nanoprecipitates, respectively. They are highlighted by the big and small red spheres.

Besides the relatively large nanoprecipitates (close to or larger than 10 nm) I have just shown, we have also observed nanopercipitates which are only several unit cells in size. Due to their small size and poor contrast with matrix, these nanoprecipitates are only visible under ultra high magnification and resolution conditions of TEM observation. A TEM image of these nanoprecipitates is shown in **Figure 3.13**, in which the cube-like and plate-like nanoprecipitates are highlighted by big and small red spheres, respectively. HRTEM images of cube-like and plate-like nanoprecipitates are shown **Figure 3.14a** and **Figure 3.14b,** respectively. The cube-like nanoprecipitates are less than 5 nm in their dimensions. And the plate-like nanoprecipitates can be only 2 atomic layers in one direction. Due to their ultra-small size and prevalence, they are thought to be possibly the energetically favorable smallest building units of nanoprecipitates in this class of materials. Possible atomic arrangements of nanoprecipitates and their nucleation mechanisms have been discussed through a collaborative HRTEM imaging, image simulation (by Dr. Lijun Wu), and a large-scale density functional theory (DFT) calculations by our collaborators at Nevada University and Oak Ridge National Laboratory.[71]

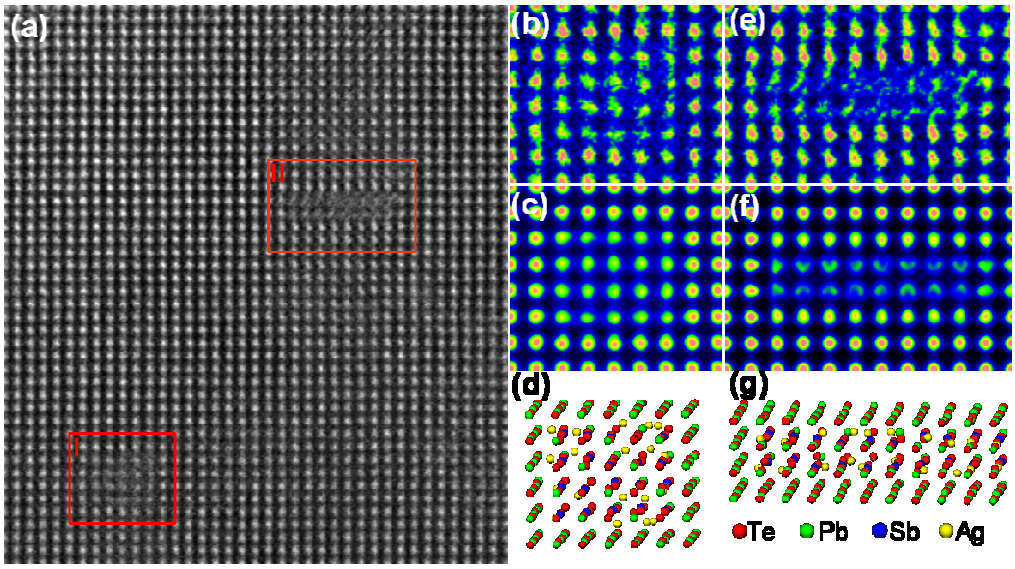

Figure 3.15 (a) Cs-corrected HRTEM image of a LAST-18 single crystal sample taken along [100] direction (by Dr. Lijun Wu). The matrix is PbTe with a lattice constant of 6.44 Å. The marked areas I and II highlight the two typical nanoprecipitates present in the sample. (b) and (e) Magnified images of I and II, respectively. (c) and (f) Corresponding simulated images based on the most stable atomic positions predicted by the DFT calculations shown in (d) and (g), respectively. The diffusive nature of the nanoprecipitates is caused by Ag atoms taking interstitial positions. For clarity, both magnified and simulated images are shown in color.[71]

The first step is to identify the detailed atomic arrangements of these ultra-small nanoprecipitates. A double Cs-corrected TEM instrument JEOL-2200MCO was employed to tackle this challenge by providing more accurate atomic positions at sub-angstrom resolution. The Cs-corrected HRTEM images of the cube-like and plate-like nanoprecipitates are shown in **Figure 3.15a**. Enlarged images of the cube-like (I) and plate-like (II) nanoprecipitates are shown in **Figure 3.15b and Figure 3.15e**, respectively, in which both nanoprecipitates show clearly diffused feature. The interpretation and determination of atomic positions from HRTEM images are collaborated by image simulation and large scale density functional theory (DFT) calculations conducted by our collaborators. Energetically favorable structural

models (**Figure 3.15d** and **Figure 3.15g)** of nanoprecipitates in LAST-18 compound were given by using large scale DFT calculations which employed a supercell containing 1728 atoms. In such a way, full-sized nanoprecipitate in real samples could be enclosed in the supercell. The simulated images **Figure 3.15c** and **Figure 3.15f** (performed by Dr. Lijun Wu**)** were obtained by using the atomic positions from DFT calculations, from which distinct deviations of atomic positions from their ideal sites to interstitial positions were revealed. Such a feature agrees well with the diffused contrast in our HRTEM observations of both cube-like (**Figure 3.15b)** and plate-like (**Figure 3.15c)** nanoprecipitates. The structural features such as size, shape, orientation, and atomic position deviations obtained from DFT calculations are corroborated by HRTEM observations. The cube-like and plate-like nanoprecipitates are in quantitative agreement with the energetically favorable smallest building units of larger nanoprecipitates in LAST-18 samples. DFT ca the nucleation of the nanoprecipitates is suggested to be driven by energetics intrinsic to the nanocomposite via the interplay between the electric dipolar attraction and the strain energy release.[71]

3.3.6 Discussions

In the LAST-18 single crystal samples, nanoprecipitates with a wide size distribution have been observed. They are analyzed to possess different lattice parameters and crystal symmetries compared to the matrix lattices, which lead to unsymmetrical strains fields around them. Most of the nanoprecipitates share a coherent interface with the surrounding matrix, which further scatter phonons while

interfere much less with electrons. For the nanoprecipitates with sizes more than 10 nm, many other kinds of defects such as anti-phase boundaries, twin boundaries, and lattice distortions were present to compensate the lattice mismatch. These defects also produce additional interfaces and boundaries with the matrix lattice, and consequently further enhance phonon scattering and reduce κ_L. The atomic position deviations from equilibrium sites would act as point defects and efficiently scatter short-wavelength (high frequency) phonons. The extensive strain fields caused by the nanoparcipitates in matrix would break the crystal periodicity and significantly enhanced Umklapp phonon scattering process, which is the dominant phonon scattering mechanism at high temperatures. Therefore, strain fields would result in distinct reduction of κ_L at high temperatures. For LAST-18 samples, κ_L keeps decreasing with increasing temperatures (**Figure 3.3b)** and played a key role for reaching the record high *ZT* value of 2.1 around 800 K.

3.4 Conclusions

In this work, TEM/HRTEM observations and structural analysis have been conducted to study the size, shape, orientation, distribution, microstructures, atomic arrangements, and nucleation mechanism of nanoprecipitates embedded in the matrix of LAST-18 single crystals. The nanoprecipitates have varying sizes and shapes. They also have different chemical composition, lattice mismatch and strain field distribution compared to the surrounding matrix. The nanoprecipitates are usually Ag-Sb rich and share coherent interfaces with matrix. The lattice difference between

nanoprecipitates and surrounding matrix varies from less than 1% to around 10%. Anti-phase boundaries, twins, and phase separations have often been observed when the size of the nanoprecipitates becomes large. Nanoprecipitates have primitive cubic and primitive tetragonal structures, as well as body-centered tetragonal lattice with tripled lattice parameter along *c* direction. The strain field caused by the nanoprecipitates shows anisotropic and long range characteristics. The size, orientation, and deviation of atomic positions of the plate-like nanoprecipitates from TEM/HRTEM observations are in good agreement with the energetically favorable smallest building units of DFT calculations. Based on the excellent agreement of structural features from DFT calculations and HRTEM observations, the nucleation of the nanoprecipitates is suggested to be driven by energestics intrinsic to the nanocomposite via the interplay between the electric dipolar attraction and the strain energy release.

Due to the difference of the wavelengths of phonons and electrons, nanoprecipitates in the LAST-18 single crystals can selectively scatter phonons much more dominantly than electrons. Thus the LAST-18 samples possess excellent electrical properties along all temperatures. The large amounts of interfaces and boundaries of nanoprecipitates and other defects with surrounding matrix lattices provide additional phonon scattering through different processes, which results in significant reduction of κ_L along the measuring temperatures.

4. Microstructure investigation of non-equilibrium synthesized p-type filled skutterudite $CeFe_4Sb_{12}$

4.1 Introduction

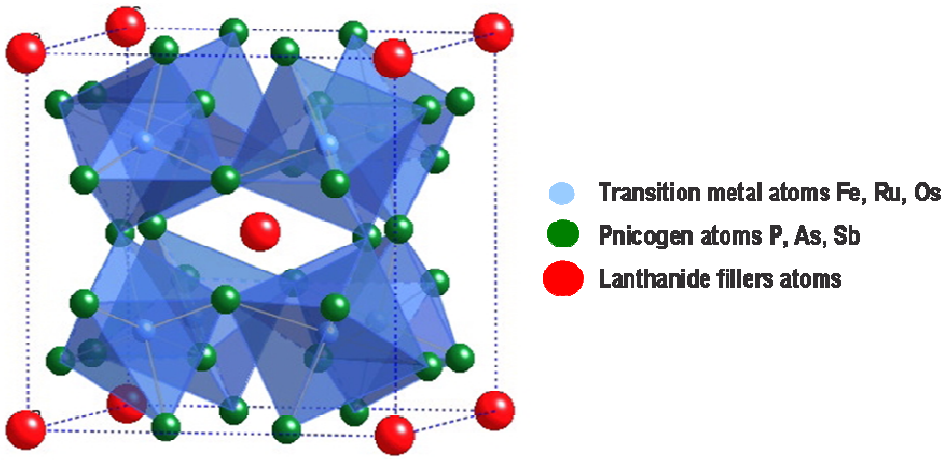

Figure 4.1 Atomic structural model of the filled skutterudite compounds, in which the green, blue, and red spheres represent the pnicogen atoms, transition metals atoms and lanthanide filler atoms, respectively.[72]

Filled skutterudites crystallize in body centered cubic (BCC) structure. The atomic structural model[72] is illustrated in **Figure 4.1**, in which the blue, green, and red spheres represent the transition metal atoms, pnicogen atoms, and rare earth atoms, respectively. Transition metal atoms are located at the center of distorted octahedra formed by pnicogen atoms. Rare earth atoms are situated at the center of cages formed by 12 pnicogen atoms. The weakly bound rare earth atoms will “rattle” about their equilibrium positions and are called “rattlers”. These “rattlers” are thought to be effective in scattering acoustic phonons which carry most of the heat in thermoelectric solids.

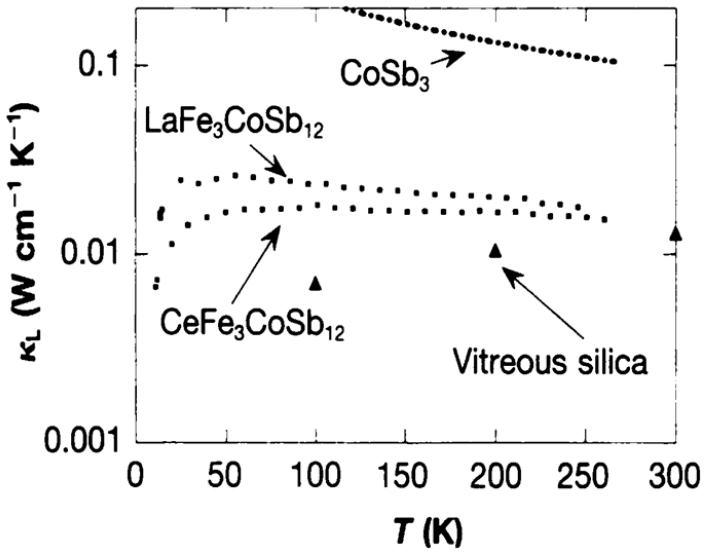

Figure 4.2 Lattice thermal conductivity as the function of temperature for $LaFe_3CoSb_{12}$, $CeFe_3CoSb_{12}$, $CoSb_3$, and vitreous silica.[17]

The binary skutterudite antimonide $CoSb_3$ exhibits excellent electrical transport properties, while its thermal conductivity is too high for it to be a good thermoelectric material.[73-74] The lattice thermal conductivities κ_L of filled skutterudites can be significantly reduced through the introduction of "rattlers", such as rare earths[17-19, 39], alkalines[75-76], or alkaline earths[41, 77]. **Figure 4.2** shows the lattice thermal conductivity dependence on temperatures of binary skutterudite $CoSb_3$, filled skutterudites $LaFe_3CoSb_{l2}$ and $CeFe_3CoSb_{l2}$ and vitreous silica.[17] It can be seen that the lattice thermal conductivities of filled skutterudites $LaFe_3CoSb_{l2}$ and $CeFe_3CoSb_{l2}$ have been reduced by near one order of magnitude compared with unfilled $CoSb_3$. At room temperature, κ_L almost reaches a value similar to that of vitreous silica. This proves that the scattering of phonons by the rattling of rare-earth ions effectively reduces κ_L in the filled skutterudite compounds and makes them promising

thermoelectric materials. The overall *ZT* values of $LaFe_3CoSb_{12}$ and $CeFe_3CoSb_{12}$ were increased to 1 at 800 K, which was among the highest values in 1996.

Filled skutterudites are model materials obeying the phonon glass electron crystal (PGEC) paradigm.[37] Due to their high chemical and mechanical stability at intermediate temperatures and the availability of both n-type and p-type materials with relatively high *ZT* values, they are among the most promising thermoelectric materials candidates for waste heat recovery in the automotive industry.[78] Consequently, approaches to prepare filled skutterudites with further reduced thermal conductivity, while maintaining good electronic properties, are always a high priority in the thermoelectric materials research. Multiple filling with selected two or three kinds of rattlers to scatter a wide spectrum of phonons has been proven to be an effective way of further reducing the thermal conductivity and subsequently enhancing *ZT* values.[79-82] A high *ZT* value of 1.34 at 800 K has been obtained in n-type triple-filled skutterudite $Ba_{0.08}Yb_{0.14}Eu_{0.1}Co_4Sb_{12}$.[80] In addition, filled skutterudite composites with secondary phase particles such as oxides[43, 83] or fullerenes[84] prepared by *in-situ* reaction method or other solid state reaction methods sometimes exhibit enhanced thermoelectric properties than the matrix materials. For example, $Yb_{0.25}Co_4Sb_{12}$ with *in-situ* formed Yb_2O_3 particles exhibit a high *ZT* value of 1.3 at 850 K.[43]

More recently, a non-equilibrium synthesis method which combines rapid solidification by melt spinning with subsequent spark plasma sintering (SPS) or hot

press has been successfully employed in the preparation of filled skutterudites[85-88] and several other bulk materials[89-91] showing markedly improved thermoelectric properties. The melt spinning process allows the formation of fine-grained or amorphous microstructure through rapidly quenching a molten alloy at extremely high cooling rates. The cooling rates achievable are on the order of 10^4–10^7 K/s. Spark plasma sintering is a relatively new sintering technique, which enables very high heating or cooling rates (up to 600 K/min), hence the sintering process is very fast, which is generally within a few minutes. This ensures the SPS process has the potential of densifying powders with nanometer sizes and nanoscale substructures by avoiding coarsening which accompanies most standard densification routes. The SPS process was conducted by our collaborators at General Motors R&D Center for this work. As a so-what similar method, hot pressing is also capable of reducing sintering temperature and shortening sintering time with applied pressure in the sintering process. A melt spinner and a DC current hot press system at BNL were used in this work as well. In both cases, the melt spinning process produces thermodynamically metastable, amorphous or ultrafine grained ribbons, which were easily compacted into stable pellets in short sintering periods under pressure by SPS or hot press.

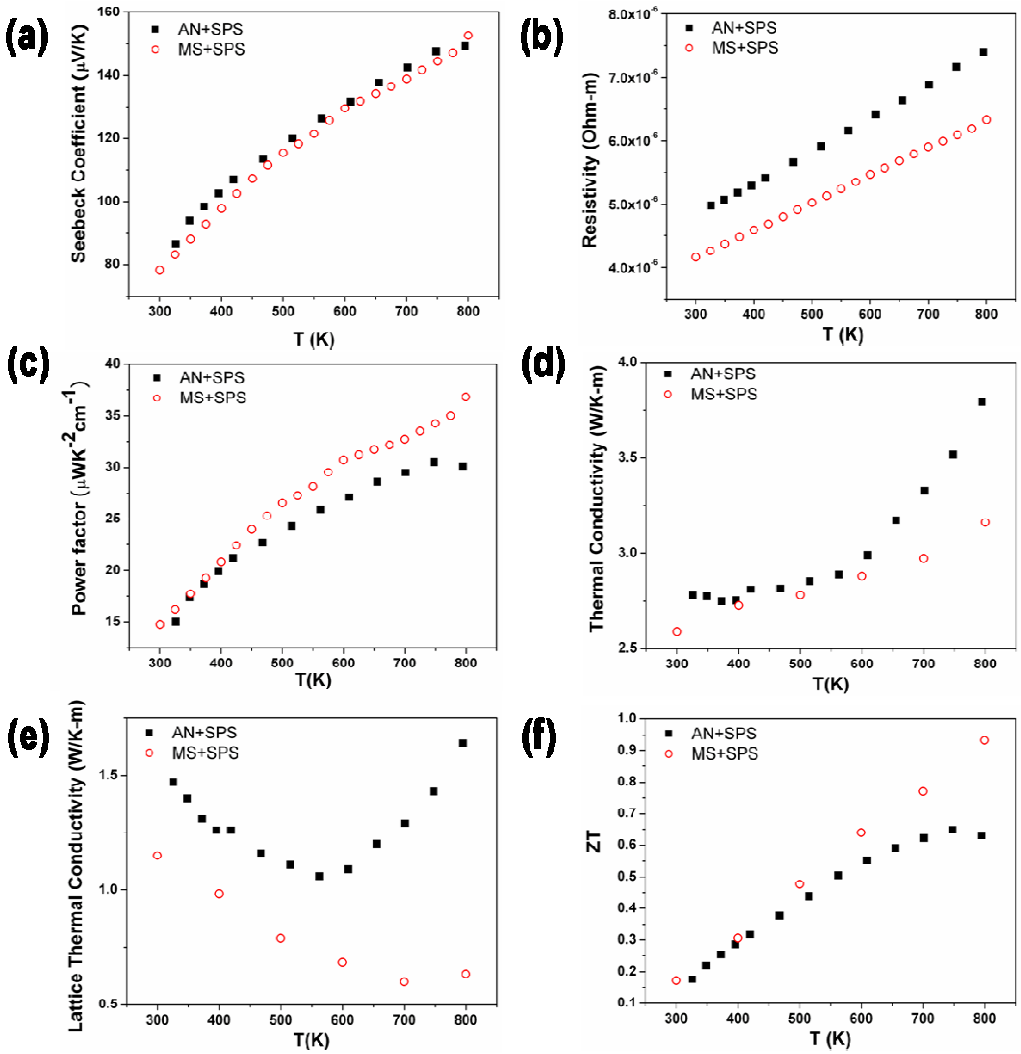

Figure 4.3 Temperature dependence of Seebeck coefficient (a), electrical resistivity (b), power factor (c), thermal conductivity (d), lattice thermal conductivity (e), and *ZT* (f) of $CeFe_4Sb_{12}$ bulk samples prepared by the non-equilibrium method and the conventional method from 300 to 800 K.[92]

The variations of Seebeck coefficient *S*, electrical resistivity ρ, power factor S^2/ρ, thermal conductivity κ, lattice thermal conductivity κ_L and figure of merit ZT as a function of temperatures of $CeFe_4Sb_{12}$ samples prepared by both the non-equilibrium and conventional methods are shown in **Figure 4.3**. The two samples have comparable Seebeck coefficient *S* values (**Figure 4.3a**), while the electrical resistivities ρ of the non-equilibrium synthesized sample are at least 25% lower than

those of conventionally synthesized samples along the measurement temperature range from 300 to 800 K (**Figure 4.3b**). This leads to higher power factor in the non-equilibrium synthesized sample (**Figure 4.3c**). The lattice thermal conductivities κ_L of the non-equilibrium synthesized samples are significantly lower than the conventionally synthesized samples (**Figure 4.3e)**. The differences of κ_L of the two kinds of samples are also getting more dominant at high temperatures with the maximum reduction of about 65% occurs at 800K. κ_L of the non-equilibrium synthesized $CeFe_4Sb_{12}$ samples is around 0.6 $Wm^{-1}K^{-1}$ at 800 K, which is the lowest value obtained in this material. The highest *ZT* value obtained from the non-equilibrium samples is 0.94 at 800 K, which is more than 50% higher than that of the conventionally synthesized samples (**Figure 4.3f)**.

The non-equilibrium synthesized p-type filled skutterudites $CeFe_4Sb_{12}$, $CeFe_3CoSb_{12}$ and other samples have been shown to have significantly improved electrical and thermal transport properties compared to samples prepared by conventional solid state reaction and long term annealing methods.[85-86] In this part of work, a comparative microstructure investigation of the $CeFe_4Sb_{12}$ samples prepared by both the non-equilibrium and conventional methods *via* X-ray diffraction (XRD), scanning electron microscopy (SEM), energy dispersive spectroscopy (EDS) and transmission electron microscopy (TEM) have been conducted to study the microstructural origins for the remarkably improved thermoelectric properties in the non-equilibrium synthesized samples, with the goal of establishing a correlation between the microstructures, materials synthesis and thermoelectric properties.

4.2 Materials synthesis

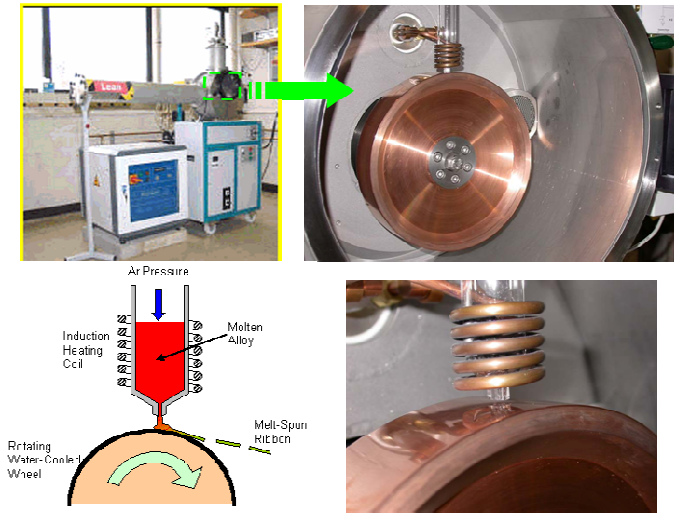

Figure 4.4 Schematic of the melt spinning system at BNL.

For the preparation of $CeFe_4Sb_{12}$ bulk materials by the non-equilibrium method, stoichiometric high purity element pieces of Ce (99.8%), Fe (99.98%) and Sb (99.9999%) were loaded into boron nitride (BN) tubes, which were then pumped and refilled with argon. The raw materials were melted at about 1450 °C for 30 seconds in an induction furnace, and then cooled down to room temperature in 30 minutes. In the next step, the ingots went through the melt spinning process to obtain very thin ribbons. A schematic of the melt spinning system at BNL is shown in **Figure 4.4**. The obtained ingot was put into a quartz tube with a 0.5 mm diameter nozzle. The ingots were melted and injected under an Ar pressure of 0.067 MPa onto a copper wheel rotating at a linear speed of 30 m/s. The collected ribbons were pressed into pellets and densified under 50 MPa at 600 °C for 2 minutes in vacuum in the SPS system.

The conventional $CeFe_4Sb_{12}$ samples were prepared by loading high purity element pieces into a quartz tube with carbon coating. The vacuumed and then sealed

quartz tube was heated to 600 °C at 2 °C/min, held for 3 hours, and slowly heated to 1050 °C at 0.5 °C/min. After holding at 1050 °C for 30 hours, the quartz tube was removed from the furnace and quenched into a water bath. It was then annealed at 700 °C for 30 hours. The ingot was removed from the quartz tube, ground to powders and followed by the same SPS procedure as that used for the non-equilibrium synthesis.

4.3 Results and discussion

4.3.1 Microstructures overview of the ribbons and the bulk samples

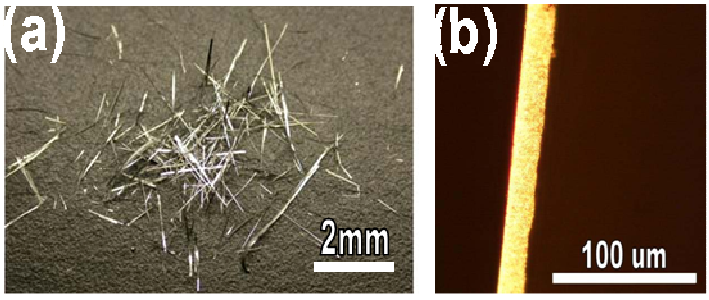

Figure 4.5 (a) Collected $CeFe_4Sb_{12}$ melt-spun ribbons; (b) Optical micrograph showing the thickness of a typical ribbon.

Melt spinning is a typical kind of rapid solidification technique. The very high cooling rate (10^4-10^7 K/s) enables the formation of microstructures with refined grain sizes, increases the solubility of alloying elements and impurities, reduces the levels of second phase segregation, and forms metastable crystalline and amorphous phases.[93] For thermoelectric applications, these effects are beneficial in the preparation of homogeneous bulk materials with improved properties. Usually, the morphology and microstructure of melt-spun ribbons are remarkably influenced by

the cooling rates of the melt spinning process. The cooling rates are controlled by several processing parameters such as wheel speed, gas pressure, melt temperature and nozzle-wheel gap etc.

In this work, ribbons with desirable microstructures have been produced repeatedly by using the optimized process parameters. The picture of a collection of the melt-spun $CeFe_4Sb_{12}$ ribbons is shown in **Figure 4.5a**. The thickness of the melt-spun ribbons can be easily measured using optical microscopy. One of the optical micrographs is shown in **Figure 4.5b**. Typical melt-spun ribbons have characteristic lengths of 5 mm and thicknesses of 15 μm.

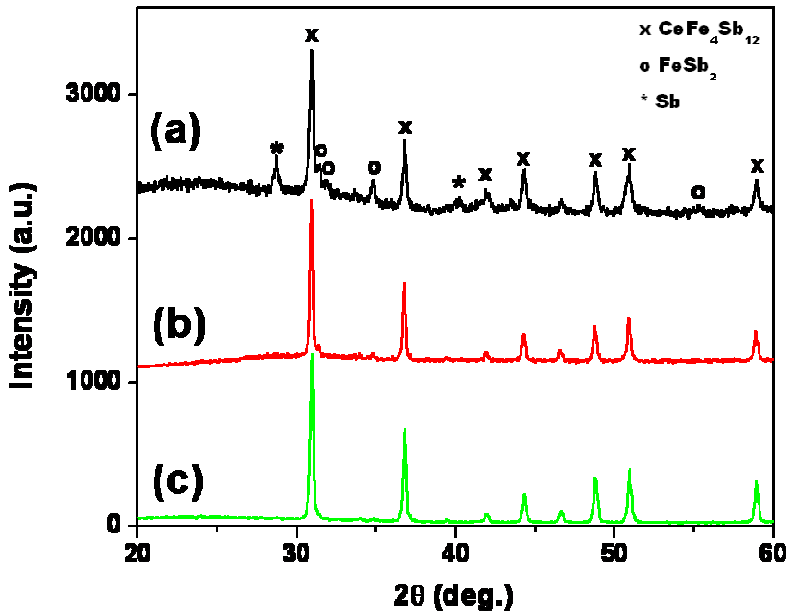

Figure 4.6 XRD patterns of (a) $CeFe_4Sb_{12}$ melt-spun ribbons and (b-c) non-equilibrium synthesized and conventionally synthesized $CeFe_4Sb_{12}$ bulk samples after spark plasma sintering.

X-ray powder diffraction (XRD) was carried out in order to investigate the crystal structure and phase composition of melt-spun ribbons, as well as those of the sintered bulk samples by the non-equilibrium and conventional methods (**Figure 4.6**).

All reflection peaks of the XRD pattern of the melt-spun ribbons (**Figure 4.6 a**) are well broadened most possibly due to the formation of ultra fine grains or even amorphous phase by the melt spinning process. The ribbons are confirmed to be comprised of mostly body-centered cubic (BCC) $CeFe_4Sb_{12}$ phase (space group Im3) with small amounts of $FeSb_2$ and Sb impurity phases. The XRD patterns of both kinds of sintered bulk samples (**Figure 4.6 b and Figure 4.6 c)** are composed of intense and sharp reflection peaks. In addition, antimony peaks appearing in the XRD pattern of the melt-spun ribbons (**Figure 4.6 a**) are not observed in the patterns of sintered bulk samples (**Figure 4.6 b** and **Figure 4.6 c**). These observations indicate that all materials have been fully reacted and crystallized in the very short SPS sintering time of 2 minutes. No obvious differences are observed from the XRD patterns of the sintered samples.

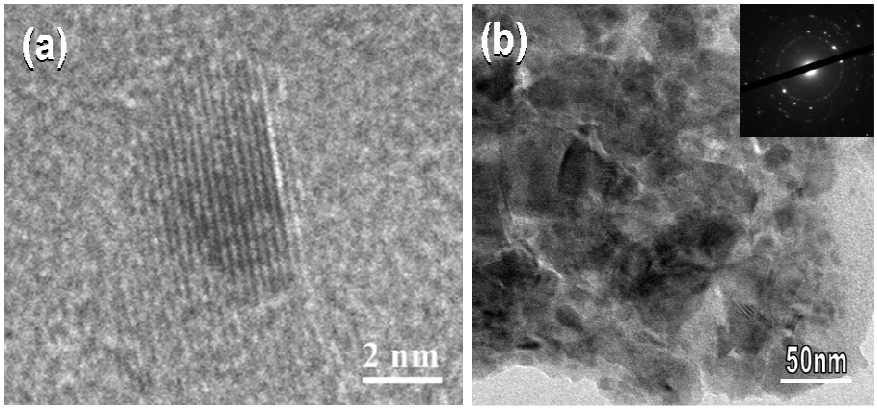

Figure 4.7 (a) HRTEM image showing a nanocrystal embedded in the amorphous matrix of a melt-spun ribbon; (b) TEM image and electron diffraction pattern in the inset showing grains of nanocrystalline nature in the melt-spun ribbons.

Amorphous phase has been observed in part of the ribbons (**Figure 4.7a**), while most of the ribbons show a nanocrytalline nature from extensive TEM imaging

and electron diffraction analysis (**Figure 4.7b**). The grain sizes in the ribbons range from several nanometers to around 50 nm.

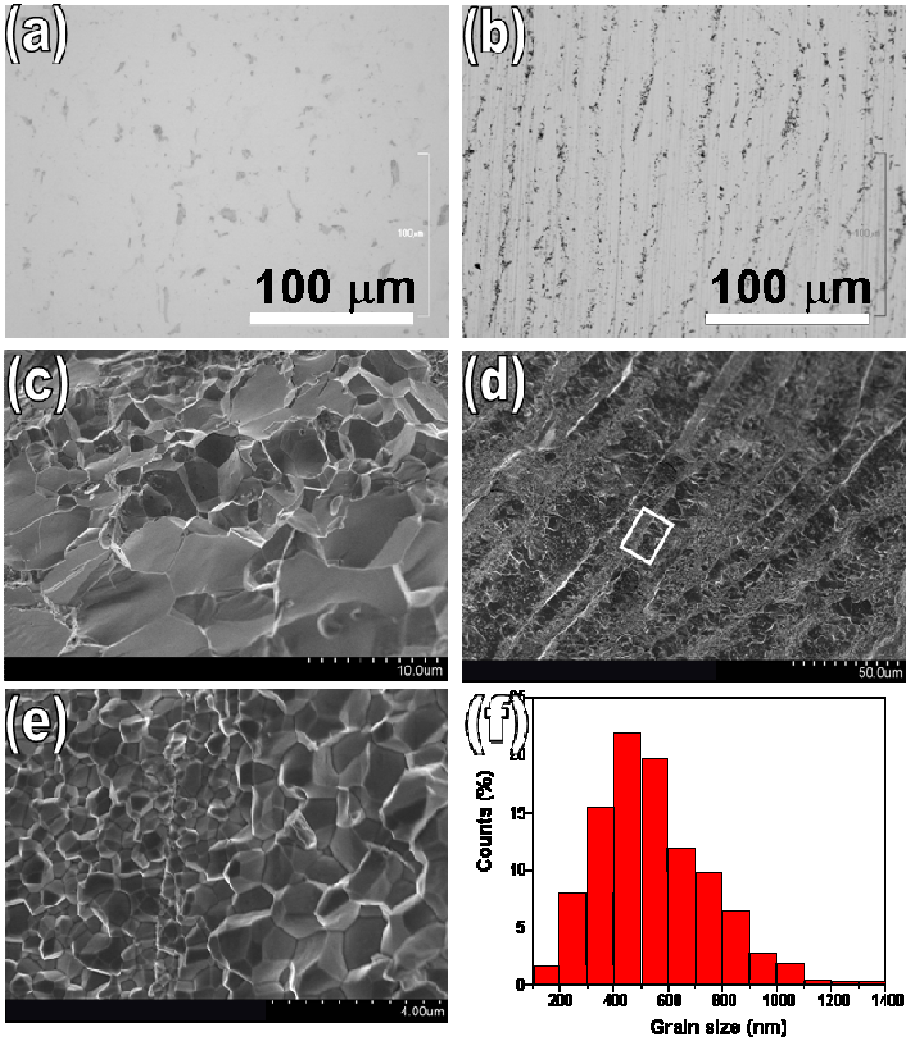

Figure 4.8 (a) and (b) Optical microscope images of fine-polished surfaces of the conventionally and non-equilibrium synthesized $CeFe_4Sb_{12}$ sample, respectively; (c) and (d) Corresponding SEM images of the fresh fracture surfaces of the conventionally and non-equilibrium synthesized $CeFe_4Sb_{12}$ sample, respectively; (e) Magnified SEM image of the rectangular box area in (d); (f) Grain size distribution histogram of the non-equilibrium synthesized $CeFe_4Sb_{12}$ samples.

Both optical micrographs and SEM images reveal the big difference of microstructures in the non-equilibrium synthesized and conventionally synthesized $CeFe_4Sb_{12}$ bulk samples. The non-equilibrium synthesized samples are composed of

compact stacking ribbon-like layers (**Figure 4.8b** and **Figure 4.7d**), while the conventionally-synthesized samples do not have such a stacking-layered structure (**Figure 4.7a** and **Figure 4.7c**). The SEM image in **Figure 4.7c** also shows the grain size of the conventionally synthesized samples varying from 1 μm to more than 10 μm. **Figure 4.7e** is a magnified SEM image of the rectangular box area in **Figure 4.7d**, which displays the contrast in the stacking layers of the non-equilibrium synthesized samples. These are caused as a result of the alternate distribution of grains with different sizes. The grain size distribution histogram retrieved from TEM images of more than 1000 grains of the non-equilibrium synthesized samples is shown in **Figure 4.7f**, which exhibit a grain size distribution from 100 nm to about 1 μm. Based on this information, it is found that the average grain size of the non-equilibrium synthesized samples is at least an order of magnitude smaller than that of the conventionally synthesized samples. Macroscopically, the non-equilibrium synthesized samples are locally comprised of modulated structures formed by grains of different sizes. Nanometer-sized and modulated-distributed grains in the non-equilibrium synthesized $CeFe_4Sb_{12}$ samples introduce much higher density of grain boundaries which can scatter a large spectrum of phonons with mean free paths comparable to or greater than the grain size. Therefore, they are able to significantly reduce the lattice thermal conductivity and enhance *ZT* values.

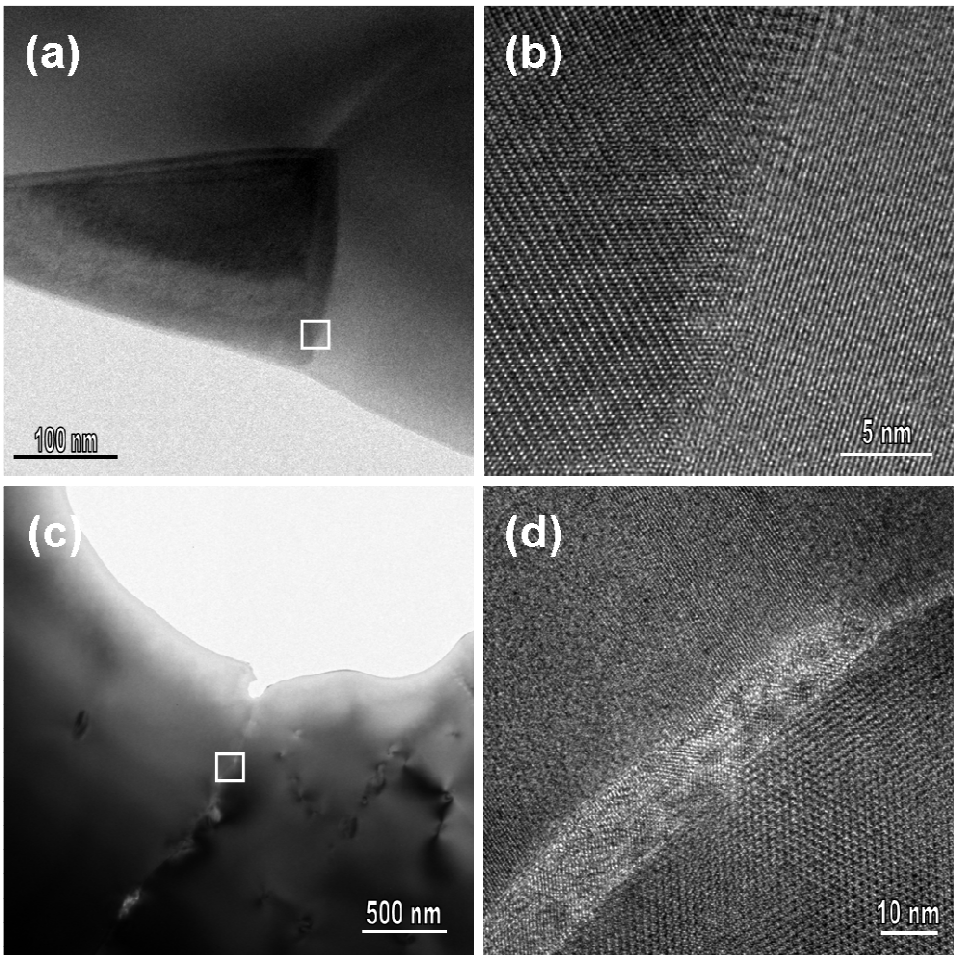

Figure 4.9 (a) and (c) Low magnification TEM images showing the typical grains and grain boundaries in the non-equilibrium and conventionally synthesized $CeFe_4Sb_{12}$ samples, respectively; (b) and (d) Magnified TEM images of the grain boundaries in the box areas in (a) and (c), respectively.

It is known that not only the density, but also the quality of the grain boundaries has a substantial influence on the electrical and thermal transport properties of a polycrystalline material. HRTEM imaging has been conducted to study the detailed grain boundaries microstructures of both sintered bulk materials (**Figure 4.9**). In the non-equilibrium synthesized $CeFe_4Sb_{12}$ samples, grains are densely packed and most of the grain boundaries are clean and straight, as shown in **Figure 4.9a**. In contrast to the non-equilibrium synthesized samples, secondary phase precipitations are easily found on the grain boundaries of the conventionally

synthesized samples, of which a typical one is shown in **Figure 4.9c**. Magnified HRTEM images of the boxed areas in **Figure 4.9a** and **Figure 4.9c** are shown in **Figure 4.9b** and **Figure 4.9d**, respectively, which display the detailed local grain boundary structures at the atomic scale. **Figure 4.9b** shows two well-coupled grains with structurally intact grain boundary in a non-equilibrium synthesized sample. However, **Figure 4.9d** shows poorly coupled grains with secondary phase precipitations on the grain boundary of a conventionally prepared sample. The widths of the secondary phase precipitation layer on the grain boundaries range from 1 to 10 nm.

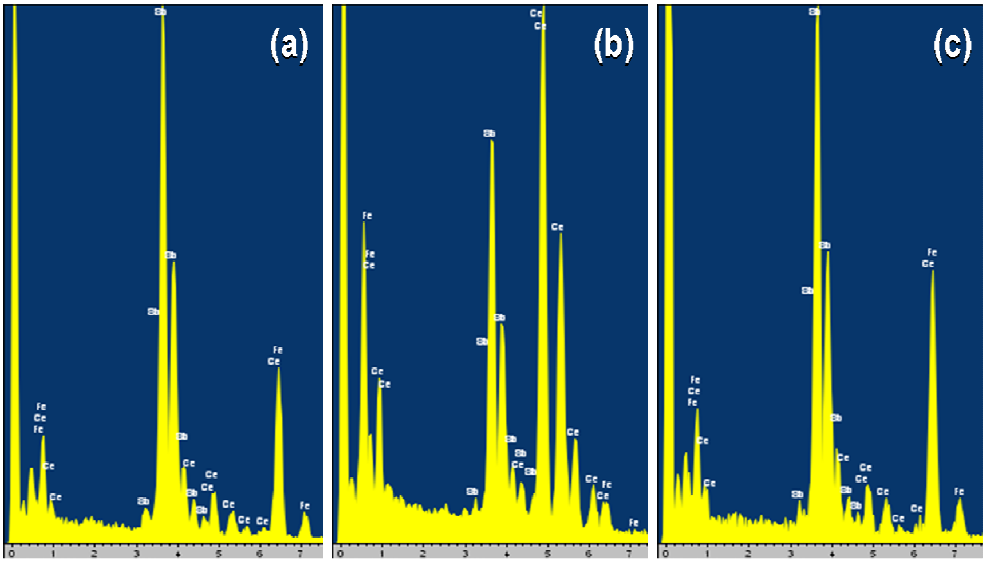

Figure 4.10 EDS line scan across a grain boundary. Spectrums (a) and (c) were taken from intragrain areas, and (b) was taken on the grain boundary.

The atomic percentages of the component elements at the grain boundaries and within the grains of the conventionally synthesized $CeFe_4Sb_{12}$ were determined by EDS. It is found that the grain boundaries are much more Ce-rich (as much as 5 to 10 times higher) than the intra-grain regions (**Figure 4.10**). For example, the Ce:Fe:Sb

ratios in two of the grain boundaries are 58.5 : 1.5 : 40 and 39.2 : 8.1 : 52.7 respectively, while the compositions within individual grain are very close to stoichiometric $CeFe_4Sb_{12}$ with ratio of 5.9 : 23.5 : 70.6.

There have been many reports suggesting that nanoprecipitates play an important role in enhancing phonon scattering and therefore reducing the thermal conductivity.[30, 35, 63, 65] Combined TEM/HRTEM imaging with chemical composition, lattice mismatch and strain field analysis have been conducted to understand the influence of the nanoprecipiates on the phonon and carrier transport properties of the non-equilibrium synthesized $CeFe_4Sb_{12}$ samples in this work.

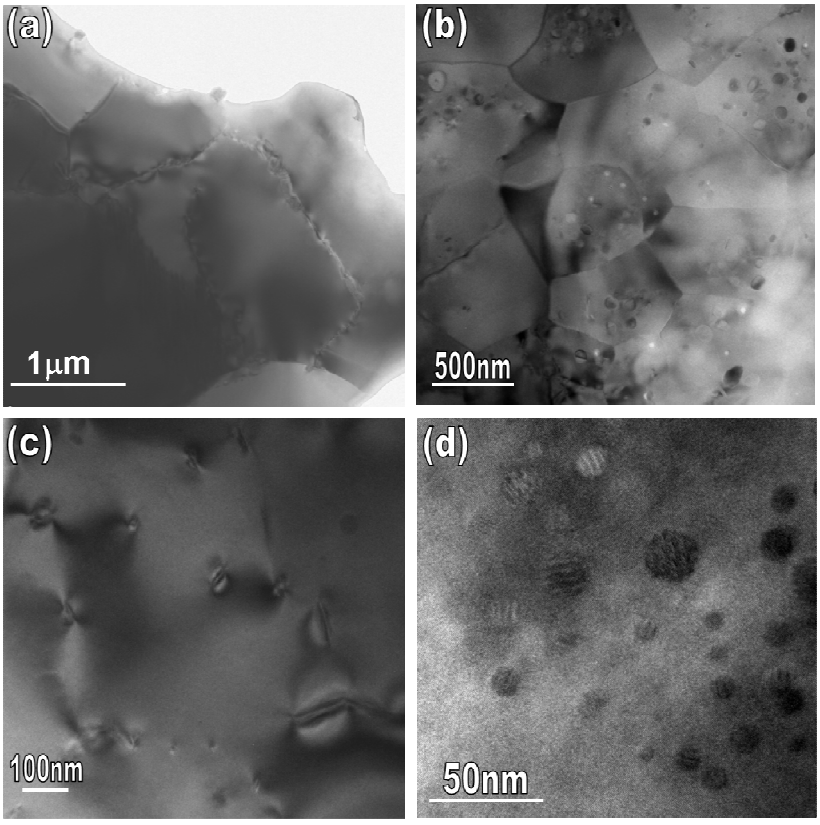

Figure 4.11 (a) Low magnification TEM images shows grains and grain boundaries of a conventionally synthesized $CeFe_4Sb_{12}$ sample; (b) Low magnification TEM image shows grains embedded with abundant nanoprecipitates in the non-equilibrium synthesized $CeFe_4Sb_{12}$ sample; (c) and (d)

TEM images at higher magnifications show the presence of intragrain dislocations and the nanoprecipitates with different sizes embedded in the grains of non-equilibrium synthesized $CeFe_4Sb_{12}$ samples, respectively.

The grains of the conventionally-synthesized $CeFe_4Sb_{12}$ samples have characteristic sizes above 1 μm and are connected by rough boundaries. No nanometer scale substructures have been observed within the grains (**Figure 4.11a**). Contrarily, individual grains with extensive nanostructures were readily observed in the non-equilibrium synthesized samples. The most common nanostructures are nanoprecipitates embedded in the matrix grains, intragrain dislocations and low angle grain boundaries (**Figure 4.11b** and **Figure 4.11c**). TEM image in **Figure 4.11d** demonstrates that most of the nanoprecipitates are coherently embedded in the matrix grains and have a large size distribution ranging from a few to several tens of nanometers.

4.3.2 Resolving the microstructures of nanoprecipitates in the non-equilibrium synthesized samples

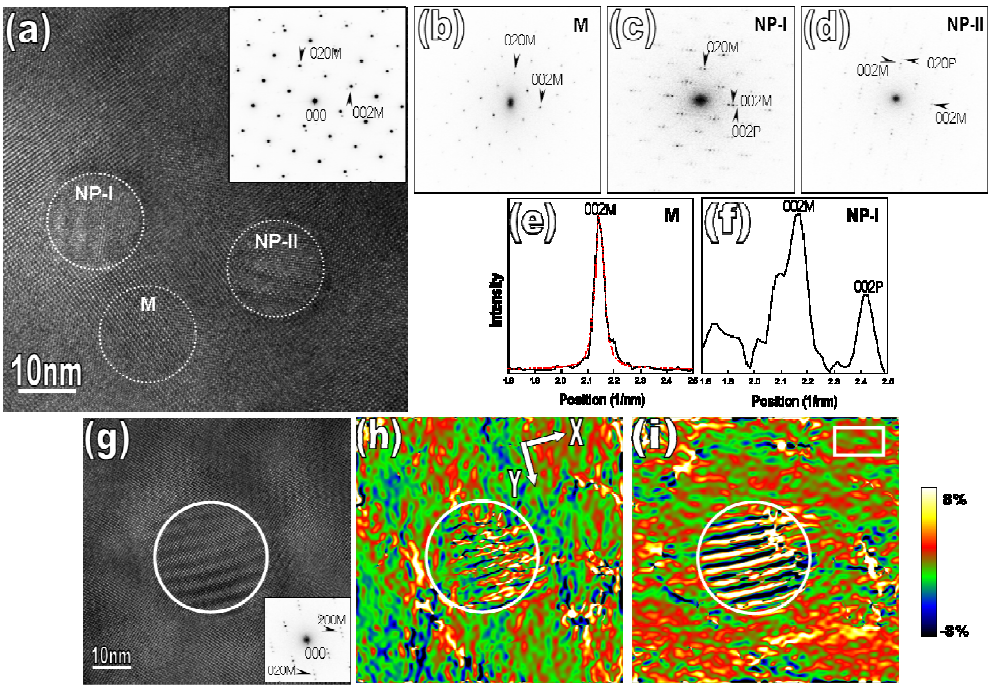

Figure 4.12 (a) HRTEM image of the non-equilibrium synthesized $CeFe_4Sb_{12}$ sample along [100] zone axis, showing two nanoprecipitates coherently embedded in the matrix. Moiré patterns are present because of the overlap of the nanoprecipitates and the matrix in the projection. The inset shows the selected area electron diffraction (SAED) pattern from the whole image. (b - d) Diffractograms of the circled matrix area M, and nanoprecipitate areas NP-I and NP-II in (a), respectively. (e) Combined Gaussian and Lorentzian fit (red dot line) to the 002 peak of the matrix (black solid line). (f) 002 peak profiles of the diffractogram of NP-I in (c). The 002 peak of NP-I shifts drastically to the right of the matrix peak, indicating that the c lattice parameter of NP-I is much smaller that that of the matrix. (g) HRTEM image showing a single nanoprecipitate for strain field analysis. (h - i) Strain-maps of ε_{xx} and ε_{yy}, which were calculated from the HRTEM image shown in (g). The white rectangle in (i) is the reference area. The maps are shown in color for clarity. The circles in the figures outline the nanoprecipitate.

The most frequently observed nanoprecipitates are around 10 nm in diameter, circular shaped and coherently embedded in the matrix with concurrence of Moiré patterns, as shown in **Figure 4.11d**. HRTEM image in **Figure 4.12a** shows two such

kind of nanoprecipitates embedded in one single grain viewed along the [100] matrix orientation. The two nanoprecipitates are about 15 nm in diameter with presence of Moiré patterns in different orientations relative to the matrix lattice. No obvious lattice distortion is observed on the interface between the nanoprecipitates and the surrounding matrix. Here we denote the two nanoprecipitates as NP-I and NP-II. Selected area electron diffraction (SAED) pattern from the whole image of **Figure 4.12a** is shown as the inset of it. The FFT diffractograms from the circled matrix area M and the nanoprecipitate areas NP-I and NP-II are shown in **Figure 4.12b**, **Figure 4.12c**, and **Figure 4.12d**, respectively. Double diffraction is less obvious in the SAED pattern, which helps us differentiate the reflection spots originating from the nanoprecipitates and the ones caused by double diffraction in the FFT diffractiograms of nanoprecipitates. Weak matrix spots appear in the FFT diffractograms of the nanoprecipitates due to the overlap of the matrix and the nanoprecipitate along the electron beam projection direction. Moiré patterns are formed for the same reason. EDS measurements show that the concentration of Sb in the nanoprecipitate areas is significantly higher than that in the neighboring matrix. Compared to the body-centered cubic structure of the matrix, excessive Sb orders along the *c* direction in the nanoprecipitates. The structure of NP-I and NP-II is determined to be primitive tetragonal. The orientation relationships between NP-I, NP-II and the surrounding matrix are $(001)_{NP\text{-}I}//(001)_M$, $(010)_{NP\text{-}I}//(010)_M$ and $(010)_{NP\text{-}II}//(001)_M$, $(001)_{NP\text{-}II}//(010)_M$, respectively. The different orientation relationships of NP-I and

NP-II with the matrix lattice result in the formation of Moiré patterns in different orientations. Specifically here, the two Moiré patterns are perpendicular to each other.

Figure 4.12e and **Figure 4.12f** are the 002 intensity profiles from the matrix and NP-I, respectively. Accurate lattice parameters are obtained by fitting the profiles using a combination of a Gaussian and a Lorentzian function. The red dot line in **Figure 4.12e** is the fitting of the 002 matrix peak. The lattice parameter of the matrix is therefore determined to be c_0 = 0.924 ± 0.003 nm. In **Figure 4.12f**, the 002 peak from NP-I shifts drastically to the right of the 002 peak from the matrix, implying that the lattice parameter c of NP-I is much smaller than that of the matrix. The lattice parameters c of NP-I and NP-II obtained by fitting the 002 peaks of the diffractograms are close to each other with c = 0.789 ± 0.005 nm. The lattice parameters a of NP-I and NP-II are equal to that of the matrix.

An HRTEM image of a single nanoprecipitate (shown in **Figure 4.12g)** is chosen for strain field analysis. This nanoprecipitate is also Sb-rich in composition, showing Moiré patterns, and has a tetragonal structure. GPA software is used to retrieve the distribution of the strain field, which is a relative strain map with respect to the reference area. **Figure 4.12h** and **Figure 4.12i** show the relative strain map ε_{xx} and ε_{yy}, retrieved from the HRTEM image in **Figure 4.12g** with g_1 = 200 and g_2 = 020, and x and y-axes pointing to the [100] and [010] directions. The reference area is marked by a white rectangle in **Figure 4.12i**. The ε_{xx} map basically shows negative strain in the matrix. Near the nanoprecipitate, there is a small region showing a

positive value of ε_{xx}. The ε_{yy} map basically shows a positive strain in the matrix. The strain in the matrix is quite different from that generated by an isotropic misfitting spherical inclusion in an infinite isotropic matrix. ε_{yy} at bottom side is larger than that at top side. One possible explanation for the asymmetric strain field around the nanoprecipitate is the stain field is not only caused by the misfit between the nanoprecipitate and the matrix but also by the local fluctuation in the composition. When a nanoparticle precipitates, it consumes Sb, resulting in the stoichiometric fluctuation in the surrounding matrix. The alternate contrast in the nanoprecipitate is complicated due to the different reflection conditions in the Moiré pattern.

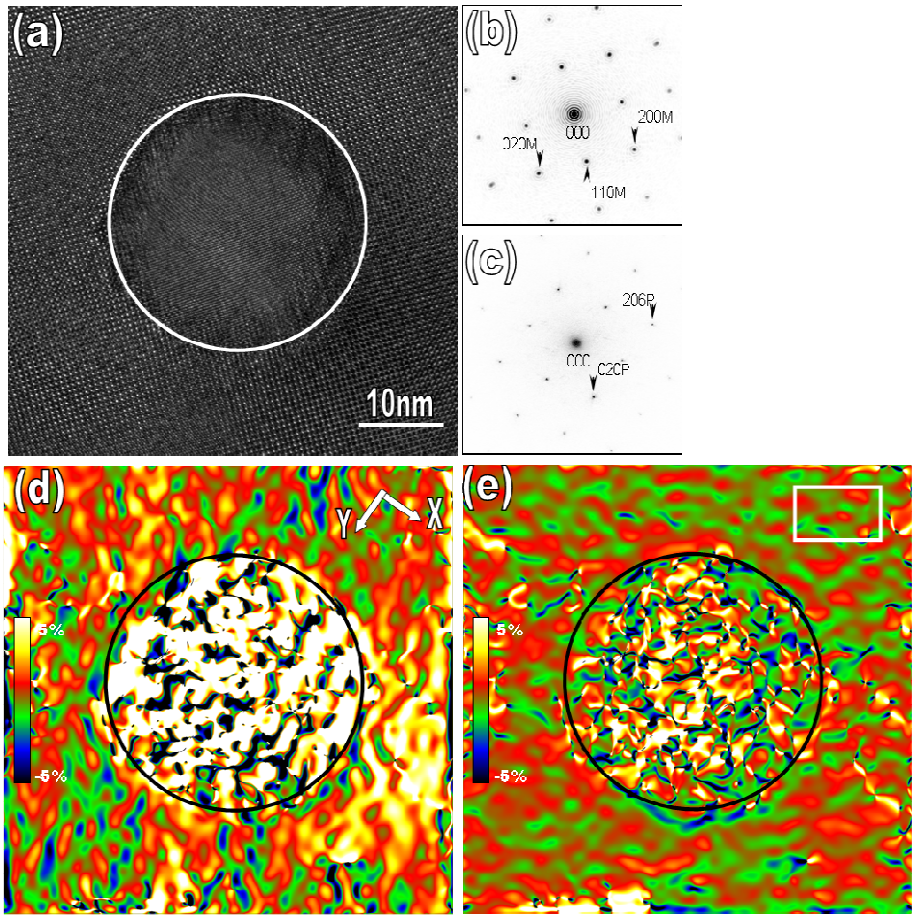

Figure 4.13 (a) HRTEM image showing a pure $CeSb_2$ nanoprecipitate embedded in the matrix of the non-equilibrium synthesized $CeFe_4Sb_{12}$ sample. Lattice distortion, antiphase boundaries and misfit dislocations are frequently observed surrounding the edge of the precipitate to compensate the differences of lattice parameters between the nanoprecipitate and the neighboring matrix. (b - c) Corresponding FFT diffractograms from the circular areas in the matrix and nanoprecipitate in (a), respectively. Strain-map of (d) ε_{xx} and (e) ε_{yy} calculated from the HRTEM image shown in (a). The white rectangle in (e) is the reference area. The maps are shown in color for clarity. The circles in the figures outline the nanoparticles.

One other typical kind of nanoprecipitates observed in the non-equilibrium synthesized $CeFe_4Sb_{12}$ samples is shown in the HRTEM image in **Figure 4.13a** along the [001] matrix direction. It is circular shaped and 30 nm in diameter. EDS analysis shows the composition of the nanoprecipitate is close to $CeSb_2$. The FFT diffractograms from the circled matrix and nanoprecipitate area are shown in **Figure**

4.13b and **Figure 4.13c**, respectively. The nanoprecipitate can be indexed as a slightly tilted $CeSb_2$ orthorhombic structure with lattice parameters a = 0.6295(6) nm, b = 0.6124(6) nm and c = 1.821(2) nm. The orientation relationship between the nanoprecipitate and the matrix is determined to be $(020)_{CeSb2}//(110)_{CeFe4Sb12}$ and $(206)_{CeSb2}//(1\text{-}10)_{CeFe4Sb12}$, respectively. A possible $CeSb_2$ phase was not detected from the X-ray diffraction pattern in **Figure 4.6 b**, which indicates only trace amounts of it may exist in the sample. In **Figure 4.13a**, lattice distortion, anti-phase boundaries and misfit dislocations are frequently observed surrounding the nanoprecipitate to compensate the differences of lattice parameters between the nanoprecipitate and the neighboring matrix.

Figure 4.13d and **Figure 4.13e** show the relative strain map ε_{xx} and ε_{yy}, retrieved from the HRTEM image in **Figure 4.13a** with g_1 = 200, g_2 = 020, and x, y axes pointing to the [100] and [010] directions. The reference area is marked by a white rectangle in **Figure 4.13e**. The ε_{xx} map shows positive strain in both the matrix and the nanoprecipitate, which is smaller at top left than that of bottom right. The ε_{yy} map shows positive strain in the nanoprecipitate and almost no strain in the matrix. ε_{yy} shows much less strain than ε_{xx}. The possible reason is part of the strains caused by the $CeSb_2$ nanoprecipitate has been released through the formation of dislocations and other defects along this direction.

4.3.3 Low angle grain boundaries in the non-equilibrium synthesized samples

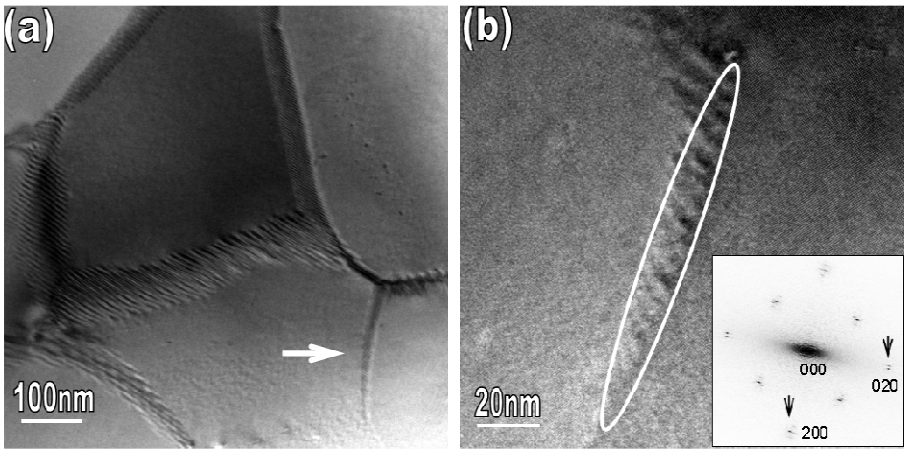

Figure 4.14 (a) Low magnification TEM image showing the presence of low angle grain boundaries in the non-equilibrium synthesized $CeFe_4Sb_{12}$ sample. (b) TEM image at a higher magnification of the grain boundary indicated by the arrow in (a) in [001] orientation. The inset shows the FFT diffractogram of the boundary area with splitting spots indicated by arrows.

Besides nanoprecipitates and intragrain dislocations, another kind of microstructural defect - low angle grain boundaries have also been observed in the non-equilibrium synthesized $CeFe_4Sb_{12}$ samples. The grain boundary indicated by the arrow in **Figure 4.14a** is shown in a higher magnification TEM image in **Figure 4.14b**. FFT diffractogram of the boundary area is shown in the inset of **Figure 4.14b**. The splitting of 200 spots (indicated by arrows) reveals that the tilt angle β equals 0.051 rad. The calculated spacing of the fringe contrast in the low angle grain boundary is $d = d_{200}/\beta$ = 4.57 Å/0.051 = 90 Å, which is in good agreement with the value measured from **Figure 4.14b**.

4.3.4 Discussions

The dominant difference of the non-equilibrium synthesis from the conventional synthesis is the replacement of the long term annealing step with melt spinning. The melt-spun ribbons are composed of nanocrystalline grains and amorphous phase due to the rapid solidification in the melt spinning process. Furthermore, phase segregation could also be effectively controlled, which results in a more homogeneous chemical distribution in the ribbons. Working as the starting materials for fast sintering under pressure, the melt-spun ribbons have much smaller sized grains and are much more homogeneous in chemical composition than the powders obtained by a lengthy ball milling procedure on annealed ingots.

Table 4.1 Microstructure differences of $CeFe_4Sb_{12}$ bulk samples prepared by the non-equilibrium and the conventional methods.

	Non-equilibrium synthesis	Conventional synthesis
Grain size	**100 nm to 1 μm**	**1 to more than 10 μm**
Grain boundary	**Atomically clean & straight**	**Rough with secondary phase**
Nanoprecipitate	**Abundant**	**None**
Low angle grain boundary	**Often observed**	**Rarely observed**
Intragrain dislocation	**Often observed**	**Rarely observed**

The subsequent SPS or hot press sintering process is very short, which does not lead to large grain size coarsening and serious phase segregation or diffusion. The small-scale local compositional inhomogeneities are activated by the thermal energy

and tend to form nanoprecipitates within the grains to reach lower system energy. These nanoprecipitates do not have enough time to diffuse to the grain boundaries. Contrarily, the long-term annealing step in the conventional synthesis provides enough time for impurity phase segregation and diffusion. Grain boundaries are often the preferred sites for the precipitation of the impurity phases. Consequently, the non-equilibrium synthesis produces samples with nanometer sized grains, cleaner grain boundaries and evenly-distributed nanoprecipitates within the grains. However, the conventional synthesis produces samples with micrometer sized grains, dirty grain boundaries with impurity phase precipitations. The non-equilibrium synthesis also produces other kinds of microstructural defects that are absent in the conventionally synthesized samples, such as intragrain dislocations and low angle grain boundaries as mentioned previously. A comparison of the microstructures of $CeFe_4Sb_{12}$ bulk samples synthesized by the non-equilibrium method and the conventional method is listed in **Table 4.1**. According to Formula 3.9, $\tau_B^{-1} = v_s / d$, the smaller the grain size, the stronger the boundaries will scatter the phonons and hinder the heat conduction. For the same composition, a polycrystalline material having a smaller average grain size usually has a smaller lattice thermal conductivity. As mentioned previously, the non-equilibrium synthesized $CeFe_4Sb_{12}$ samples are composed of nanometer sized grains with a wide size distribution. The total number of grain boundaries is dramatically increased compared to the conventionally synthesized samples with micrometer sized grains. The grain boundaries scatter phonons with mean free paths comparable to the grain size, thereby reducing the thermal conductivity. Additionally,

the wide size distribution of grains helps scatter phonons of a wide spectrum of wavelengths, which is also a beneficial factor for the enhancement of phonon scattering and the suppression of κ_L. The abundant nanoprecipitates embedded in the individual grains provide effective phonon scattering centers and introduce high intensity of interfaces and strain fields on the matrix. The other microstructural defects such as intragrain dislocations and low angle grain boundaries also produce additional interfaces with the matrix that enhance phonon scattering. Furthermore, nanoprecipitates and other microstructure defects in the non-equilibrium synthesized $CeFe_4Sb_{12}$ samples is effective in enhancing phonon scattering and leads to a much lower κ_L than that of the conventionally synthesized samples along the whole temperature range measured (**Figure 4.3e**).

As discussed, additional phonon scattering caused by the microstructure defects helps suppress κ_L of the non-equilibrium synthesized $CeFe_4Sb_{12}$ samples remarkably. For the electrical transport properties, the non-equilibrium synthesized $CeFe_4Sb_{12}$ samples show comparable S and lower ρ, and thus a higher PF, as shown in **Figure 4.3**. This result confirms that the microstructural defects have much less effects on the electrical transport properties. As has been discussed in chapter 3, because the dominate wavelength of carriers is much bigger than that of phonons, it is possible that the imperfect interfaces only limit the phonon transport, but leave the carriers transport intact. The atomically clean and straight grain boundaries in the non-equilibrium synthesized samples provide more conducive paths for the carriers, which are holes in $CeFe_4Sb_{12}$.

4.4 Conclusions

Filled skutterudite $CeFe_4Sb_{12}$ prepared by the non-equilibrium synthesis method has exhibited 50% improvement in *ZT* values over samples made by the conventional synthesis method. We attempted to understand the underlying origins for the simultaneous enhancements of both electrical and thermal transport properties in the non-equilibrium synthesized samples through a comparative microstructure study of samples prepared by both the non-equilibrium method and the conventional method. The exclusive microstructures of the non-equilibrium synthesized samples include nanometer sized grains, alternate distribution of grains with different sizes, abundant nanoprecipitates within grains, intragrain dislocations, low angle grain boundaries and other defects. These microstructures introduce high densities of interfaces and boundaries, which strongly enhances phonon scattering so as to significantly reduce κ_L. At the same time, the cleaner grain boundaries and low angle grain boundaries are beneficial factors that result in excellent electrical transport properties.

Reference

1. D. K. C. Macdonald, *Thermoelectricity: an Introduction to the Principles*. 1962, New York: John Wiley & Sons.
2. T. J. Seebeck. Abh. K. Akad. Wiss. 1823, Berlin.
3. J. C. Peltier, Ann. Chem., 1834: p. 371.
4. T. M. Tritt, and M.A. Subramanian, *Thermoelectric Materials, Phenomena, and Applications: A Bird's Eye View*. MRS Bulletin, 2006. **31**: p. 188-194.
5. G. J. Snyder. [cited 2010 Sept. 6]; Available from: http://www.thermoelectrics.caltech.edu/.
6. J. Yang, and T. Caillat, *Thermoelectric Materials for Space and Automotive Power Generation.* MRS Bulletin, 2006. **31**: p. 224-229.
7. H. J. Goldsmid, *Thermoelectric Refrigeration*. 1964, New York: Plenum Press.
8. G. D. Mahan, *Good thermoelectrics.* Solid State Physics, 1997. **51**: p. 81-157.
9. R. Franz, and G. Wiedemann, *Ueber die Wärme-Leitungsfähigkeit der Metalle* Annalen der Physik, 1853. **165**(8): p. 497-531.
10. L. D. Hicks, and M.S. Dresselhaus, *Effect of quantum-well structures on the thermoelectric figure of merit* Phys. Rev. B, 1993. **47**(19): p. 12727-12731.
11. F. J. DiSalvo, *Thermoelectric cooling and power generation.* Science, 1999. **285**(5428): p. 703-706.
12. K. F. Hsu, S. Loo, W. Chen, C. Uher, T. Hogan, and M. G. Kanatzidis, *Thermoelectric Properties of the cubic $AgPb_{10}SbTe_{12}$*. Mater. Res. Soc. symp. Proc., 2004. **793**: p. S6.3.1-S6.3.5.
13. G. S. Nolas, J. Sharp, and J. Goldsmid, *Thermoelectrics: Basic Principles and New Material Developments*. 2001: Springer.
14. G. J. Snyder, *Complex thermoelectric materials.* Nature Materials, 2008. **7**: p. 105-114.
15. Yu. I. Ravich, B. A. Efimova, and I. A. Smirnov, eds. *Semiconducting Lead Chalcogenides*. ed. L.S. Stil'bans. 1970, Plenum Press: New York.
16. C. B. Vining, W. Laskow, J. O. Hanson, R. R. Vanderbeck, and P. D. Gorsuch, *Thermoelectric properties of pressure-sintered $Si_{0.8}Ge_{0.2}$ thermoelectric alloys.* J. Appl. Phys., 1991. **69**(8): p. 4333-4340.
17. B. C. Sales, D. Mandrus, and R. K. Williams, *Filled skutterudite antimonides: A new class of thermoelectric materials.* Science, 1996. **272**: p. 1325-1328.

18. J. P. Fleurial, A. Bky, and T. Caillat, *High Figure of Merit in Ce-Filled Skutterudites*, in *15th International Conference on Thermoelectrics*, IEEE, Editor. 1996. p. 91-95.

19. G. S. Nolas, M. Kaeser, R.T. Littleton, and T.M. Tritt, *High figure of merit in partially ytterbium filled skutterudite materials.* Appl. Phys. Lett., 2000. **77**(12): p. 1855-1857.

20. R. Venkatasubramanian, T. Colpitts, E. Watko, M. Lamvik, and N. ElMasry, *MOCVD of Bi_2Te_3, Sb_2Te_3 and their superlattice structures for thin-film thermoelectric applications.* J Cryst Growth, 1997. **170**(1-4): p. 817-821.

21. T. C. Harman, P. J. Taylor, D. L. Spears, and M. P. Walsh, *Thermoelectric quantum-dot superlattices with high ZT.* J Electron Mater, 2000. **29**(1): p. L1-L4.

22. R. Venkatasubramanian, E. Siivola, T. Colpitts, and B. O'Quinn, *Thin-film thermoelectric devices with high room-temperature figures of merit.* Nature, 2001. **413**(6856): p. 597-602.

23. T. C. Harman, P. J. Taylor, M. P. Walsh, and B. E. LaForge, *Quantum dot superlattice thermoelectric materials and devices.* Science, 2002. **297**(5590): p. 2229-2232.

24. M. S. Dresselhaus, G. Chen, M. Y. Tang, R. G. Yang, H. Lee, D. Z. Wang, Z. F. Ren, J. P. Fleurial, and P. Gogna, *New directions for low dimensional thermoelectric materials.* Advanced Materials, 2007. **19**: p. 1043-1053.

25. L. D. Hicks, and M.S. Dresselhaus, *Thermoelectric figure of merit of one-dimensional conductor.* Phys. Rev. B, 1993. **47**(24): p. 16631-16634.

26. L. D. Hicks, T. C. Harman, and M. S. Dresselhaus, *Use of quantum-well superlattices to obtain a high figure of merit from nonconventional thermoelectric materials.* Appl. Phys. Lett., 1993. **63**(23): p. 3230-3232.

27. W. Kim, J. Zide, A. Gossard, D. Klenov, S. Stemmer, A. Shakouri, and A. Majumdar, *Thermal Conductivity Reduction and Thermoelectric Figure of Merit Increase by Embedding Nanoparticles in Crystalline Semiconductors.* phys. Rev. Lett., 2006. **96**(4): p. 045901 (1-4).

28. K. F. Hsu, S. Loo, F. Guo, W. Chen, J. S. Dyck, C. Uher, T. Hogan, E. K. Polychroniadis, and M. G. Kanatzidis, *Cubic $AgPb_mSbTe_{2+m}$: Bulk thermoelectric materials with high figure of merit.* Science, 2004. **303**(5659): p. 818-821.

29. M. Zhou, J. F. Li, and T. Kita, *Nanostructured AgPbmSbTem+2 System Bulk Materials with Enhanced Thermoelectric Performance.* J. Am. Chem. Soc., 2008. **130**: p. 4527-4532.

30. J. Q. He, A. Gueguen, J. R. Sootsman, J. C. Zheng, L. J. Wu, Y. M. Zhu, M. G. Kanatzidis, and V. P. Dravid, *Role of Self-Organization, Nanostructuring,*

and Lattice Strain on Phonon Transport in $NaPb_{18-x}Sn_xBiTe_{20}$ Thermoelectric Materials. J. Am. Chem. Soc., 2009 **131** (49): p. 17828-17835

31. G. A. Slack, ed. *CRC Handbook of Thermoelectrics*. ed. D.M. Rowe. 1995, CRC Press: Boca Raton.

32. B. Poudel, Q. Hao, Y. Ma, Y. C. Lan, A. Minnich, B. Yu, X. Yan, D. Z. Wang, A. Muto, D. Vashaee, X. Y. Chen, J. M. Liu, M. S. Dresselhaus, G. Chen, and Z. F. Ren, *High-Thermoelectric Performance of Nanostructured Bismuth Antimony Telluride Bulk Alloys.* Science, 2008. **320**: p. 634-638.

33. R. G. Yang, and G. Chen, *Thermal Conductivity Modeling of Periodic Two-Dimensional Nanocomposites.* Phys. Rev. B, 2004. **69**(19): p. 195316 (1-10).

34. R. G. Yang, G. Chen, and M. S. Dresselhaus, *Thermal Conductivity of Simple and Tubular Nanowire Composites in Longitudinal Direction.* Phys. Rev. B, 2005. **72**(12): p. 125418 (1-7).

35. J. Q. He, S. N. Girard, M. G. Kanatzidis, and V. P. Dravid, *Microstructure-Lattice Thermal Conductivity Correlation in Nanostructured $PbTe_{0.7}S_{0.3}$ Thermoelectric Materials.* Adv. Funct. Mater., 2010. **20**: p. 764-772.

36. D. T. Morelli, and G.P. Meisner, *Low temperature properties of the filled skutterudite $CeFe_4Sb_{12}$.* J. Appl. Phys., 1995. **77**(8): p. 3777-3781.

37. B. C. Sales, D. Mandrus, B. C. Chakoumakos, V. Keppens, and J. R. Thompson, *Filled Skutterudite Antimonides: Electron Crystals and Phonon Glasses.* Phys. Rev. B, 1997. **56**(23): p. 15081-15089.

38. G. S. Nolas, J. L. Cohn, and G. A. Slack, *Effect of partial void filling on the lattice thermal conductivity of skutterudites.* Phys. Rev. B, 1998. **58**(1): p. 164-170.

39. G. S. Nolas, G. A. Slack, D. T. Morelli, T. M. Tritt, and A. C. Ehrlich, *The effect of rare-earth filling on the lattice thermal conductivity of skutterudites.* J. Appl. Phys., 1996. **79**(8): p. 4002-4008.

40. J. S. Dyck, W. Chen, C. Uher, L. D. Chen, X. F. Tang, and T. Hirai, *Thermoelectric properties of the n-type filled skutterudite $Ba_{0.3}Co_4Sb_{12}$ doped with Ni.* J. Appl. Phys., 2002. **91**(6): p. 3698-3705.

41. L. D. Chen, T. Kawahara, X. F. Tang, a.T.H. T. Goto, IJ. S. Dyck, W. Chen, and C. Uher, *Anomalous barium filling fraction and n-type thermoelectric performance of $Ba_yCo_4Sb_{12}$.* J. Appl. Phys., 2001. **90**(4): p. 1864-1868.

42. J. Yang, G. P. Meisner, C. J. Rawn, H. Wang, B. C. Chakoumakos, J. Martin, G. S. Nolas, B. L. Pedersen, and J. K. Stalick, *Low temperature transport and structural properties of misch-metal-filled skutterudites.* J. Appl. Phys., 2007. **102**(8): p. 083702 (1-7).

43. X. Y. Zhao, X. Shi, L. D. Chen, W. Q. Zhang, S. Q. Bai, Y. Z. Pei, and X.Y. Li, *Synthesis of $Yb_yCo_4Sb_{12}/Yb_2O_3$ composites and their thermoelectric properties.* Appl. Phys. Lett., 2006. **89**(9): p. 092121 (1-3).

44. J. S. Kasper, P. Hagenmuller, M. Pouchard, and C. Cros, *Clathrate Structure of Silicon Na_8Si_{46} and Na_xSi_{136} (x < 11).* Science, 1965. **150**(3704): p. 1713-1714.

45. C. Cros, M. Pourchard, and P. Hagenmul, *2 New Clathrate Structures of Silicon and Germanium.* Bulletin de la Societe Chimique de France, 1971. **2**: p. 379.

46. G. S. Nolas, J. L. Cohn, G. A. Slack, and S. B. Schujman, *Semiconducting Ge clathrates: Promising candidates for thermoelectric applications.* Appl. Phys. Lett., 1998. **73**(2): p. 178-180.

47. C. M. Bhandari, and D. M. Rowe, *Thermal Conduction in Semiconductors*. 1988: Wiley Eastern Limited.

48. J. Callaway, *Model for lattice thermal conductivity at low temperatures.* Phys. Rev., 1959. **113**(4): p. 1046-1051.

49. J. Callaway, and H. C. Von Baeyer, *Effect on point imperfections on lattice thermal conductivity.* Phys. Rev., 1960. **120**(4): p. 1149-1154.

50. G. Chen, M. S. Dresselhaus, G. Dresselhaus, j. p. fleurial, and T. Caillat, *Recent Developments in Thermoelectric Materials.* Inter. Mater. Rev.,, 2003. **48**(1): p. 45-66.

51. C. M. Bhandari, and D. M. Rowe, *Boundary Scattering of phonons.* J. Phys. C: Solid State Phys., 1978. **11**: p. 1787-1794.

52. C. M. Bhandari, and D. M. Rowe, *Silicon-germanium alloys as high-temperature thermoelectric materials.* Contemp. Phys.,, 1980. **21**(3): p. 219 - 242.

53. Univeristy of Liverpool. [cited 2010 Sept. 6]; Available from: http://www.matter.org.uk/diffraction/x-ray/laue_method.htm.

54. M. Dudley, *Structure of Materials Lecture Notes*. 2004: Stony Brook University.

55. Carleton College. [cited 2010 Sept. 6]; Available from: http://serc.carleton.edu/research_education/geochemsheets/techniques/XRD.html,.

56. P. Scherrer, Göttinger Nachrichten Gesell, 1918. **2**: p. 98

57. A.Patterson, *The Scherrer Formula for X-Ray Particle Size Determination.* Phys. Rev. B, 1939. **56** (10): p. 978-982.

58. J. I. Goldstein, D. E. Newbury, P. Echlin, D. C. Joy, C. Fiori, and E. Lifshin, *Scanning electron microscopy and x-ray microanalysis*. 1981, New York: Plenum Press.

59. Ceter for Functional Nanomaterials, B.N.L. [cited 2010 Sept. 23]; Available from: http://www.bnl.gov/cfn/facilities/Electron_Microscopy.asp.

60. M. J. Hytch, J. L. Putaux, and J. M. Penisson, *Measurement of the displacement field around dislocations to 0.03A by electron microscopy.* Nature, 2003. **423** p. 270-273.

61. M. J. Hÿtch, E. Snoeck, and R. Kilaas, *Quantitative measurement of displacement and strain fields from HREM micrographs.* Ultramicroscopy, 1998. **74**: p. 131.

62. C. L. Johnson, M. J. Hytch, and P. R. Buseck, *Nanoscale waviness of low-angle grain boundaries.* PNAS, 2004. **101**: p. 17936-17939.

63. L. J. Wu, J. C. Zheng, J. Zhou, Q. Li, J. H. Yang, and Y.M. Zhu, *Nanostructures and Defects in Thermoelectric $AgPb_{18}SbTe_{20}$ Investigated by Quantitative High Resolution Transmission Electron Microscopy*. J. Appl. Phys., 2009. **105**(9): p. 094317 (1-8).

64. F. D. Rosi, E. F. Hockings, and N. E. Lindenblad, *Semiconducting Materials for Thermoelectric Power Generation*, in *RCA Rev.* 1961. p. 82.

65. E. Quarez, K. F. Hsu, R. Pcionek, N. Frangis, E. K. Polychroniadis, and M. G. Kanatzidis, *Nanostructuring, compositional fluctuations, and atomic ordering in the thermoelectric materials $AgPb_mSbTe_{2+m}$. The myth of solid solutions.* J. Am. Chem. Soc., 2005. **127**(25): p. 9177-9190.

66. T. J. Zhu, F. Yan, S. N. Zhang, and X. B. Zhao, *Microstructure and electrical properties of quenched $AgPb_{18}Sb_{1-x}Te_{20}$ thermoelectric materials.* J Phys D Appl Phys, 2007. **40**(11): p. 3537-3540.

67. D. I. Bilc, S. D. Mahanti, E. Quarez, K. F. Hsu, R. Pcionek, and M. G. Kanatzidis, *Resonant states in the electronic structure of the high performance thermoelectrics $AgPb_mSbTe_{2+m}$: The role of Ag-Sb microstructures.* Phys. Rev. Lett., 2004. **93**(14): p. 146403 (1-4).

68. D. I. Bilc, S. D. Mahanti, and M. G. Kanatzidis, *Electronic transport properties of PbTe and $AgPb_mSbTe_{2+m}$ systems.* Phys. Rev. B, 2006. **74**(12): p. 125202 (1-12).

69. P. F. P. Poudeu, J. D'Angelo, A. D. Downey, J. L. Short, T. P. Hogan, and M. G. Kanatzidis, *High Thermoelectric Figure of Merit and Nanostructuring in Bulk p-type $Na_{1-x}Pb_mSb_yTe_{m+2}$*. Angew. Chem. Int. Ed., 2006. **45**: p. 3835 -3839.

70. P. F. P. Poudeu, J. D'Angelo, H. J. Kong, A. Downey, J. L. Short, R. Pcionek, T. P. Hogan, C. Uher, and M. G. Kanatzidis, *Nanostructures versus Solid Solutions: Low Lattice Thermal Conductivity and Enhanced Thermoelectric Figure of Merit in $Pb_{9.6}Sb_{0.2}Te_{10-x}Se_x$ Bulk Materials.* J. Am. Chem. Soc., 2006. **128**: p. 14347-14355.

71. X. Z. Ke, C. F. Chen, J. Yang, L. J. Wu, J. Zhou, Q. Li, Y. M. Zhu, and P.R. Kent, *Microstructure and a Nucleation Mechanism for Nanoprecipitates in PbTe-AgSbTe$_2$*. Phys. Rev. Lett., 2009. **103**(14): p. 145502 (1-4).

72. B. C. Sales, *Filled Skutterudites*, in *Handbook on the Physics and Chemistry of the Rare Earths*. 2002.

73. D. T. Morelli, T. Caillat, J. P. Fleurial, A. Borshchevsky, J. Vandersande, B. Chen, and C. Uher, *Low-Temperature Transport-Properties of P-Type CoSb$_3$*. Phys. Rev. B, 1995. **51**(15): p. 9622-9628.

74. J. W. Sharp, E. C. Jones, R. K. Williams, P. M. Martin, and B. C. Sales, *Thermoelectric Properties of CoSb$_3$ and Related Alloys.* J. Appl. Phys., 1995. **78**(2): p. 1013-1018.

75. Y. Z. Pei, J. Yang, L. D. Chen, W. Zhang, J. R. Salvador, and J. H. Yang, *Improving thermoelectric performance of caged compounds through light-element filling.* Appl. Phys. Lett., 2009. **95**(4): p. 042101 (1-3).

76. Y. Z. Pei, L. D. Chen, W. Zhang, X. Shi, S. Q. Bai, X. Y. Zhao, Z. G. Mei, and X. Y. Li, *Synthesis and thermoelectric properties of K$_y$Co$_4$Sb$_{12}$*. Appl. Phys. Lett. , 2006. **89**: p. 221107 (1-3).

77. X. Y. Zhao, X. Shi, L. D. Chen, W. Q. Zhang, W. B. Zhang, and Y. Z. Pei, *Synthesis and thermoelectric properties of Sr-filled skutterudite Sr$_y$Co$_4$Sb$_{12}$*. J. Appl. Phys., 2006. **99**(5): p. 053711 (1-4).

78. J. Yang, *Potential Applications of Thermoelectric Waste Heat Recovery in the Automotive Industry*. International Conference on Thermoelectrics, 2005: p. 155.

79. X. Shi, H. Kong, C. P. Li, C. Uher, J. Yang, J. R. Salvador, H. Wang, L. Chen, and W. Zhang, *Low thermal conductivity and high thermoelectric figure of merit in n-type Ba$_x$Yb$_y$Co$_4$Sb$_{12}$ double-filled skutterudites.* Appl. Phys. Lett., 2008. **92**(18): p. 182101 (1-3).

80. X. Shi, J. R. Salvador, J. Yang, and H. Wang, *Thermoelectric Properties of n-Type Multiple-Filled Skutterudites.* J. Electron. Mater., 2009. **38**(7): p. 930.

81. J. Yang, W. Zhang, S. Q. Bai, Z. Mei, and L. D. Chen, *Dual-frequency resonant phonon scattering in Ba$_x$R$_y$Co$_4$Sb$_{12}$ (R=La, Ce and Sr).* Appl. Phys. Lett., 2007. **90**(19): p. 192111 (1-3).

82. S. Q. Bai, Y. Z. Pei, L. D. Chen, W. Q. Zhang, X. Y. Zhao, and J. Yang, *Enhanced thermoelectric performance of dual-element-filled skutterudites Ba$_x$Ce$_y$Co$_4$Sb$_{12}$.* Acta Mater, 2009. **57**: p. 3135-3139.

83. Z. Xiong, X. H. Chen, X. Y. Zhao, S. Q. Bai, X. Y. Huang, and L. D. Chen, *Effects of nano-TiO$_2$ dispersion on the thermoelectric properties of filled-skutterudite Ba$_{0.22}$Co$_4$Sb$_{12}$.* Solid State Sciences, 2009. **11**: p. 1612-1616.

84. X. Shi, L. D. Chen, S. Q. Bai, X. Y. Huang, X. Y. Zhao, Q. Yao, and C. Uher, *Influence of fullerene dispersion on high temperature thermoelectric properties of $Ba_yCo_4Sb_{12}$-based composites.* J. Appl. Phys., 2007. **102**(10): p. 103709 (1-7).

85. Q. Li, Z. W. Lin, and J. Zhou, *Thermoelectric Materials with Potential High Power Factors for Electricity Generation.* J Electron Mater, 2009. **38**(7): p. 1268-1272.

86. Q. Jie, J. Zhou, I. K. Dimitrov, C. P. Li, C. Uher, H. Wang, W. Porter, and Q. Li, *Thermoelectric Properties of Non-equilibrium Synthesized $Ce_{0.9}Fe_3CoSb_{12}$ Filled Skutterudites* Mater. Res. Soc. Symp. Proc., 2010. **1267**: p. DD03-03.

87. J. Zhou, Q. Jie, and Q. Li, *Microstructure of non-equilibrium synthesized p-type Filled Skutterudite $CeFe_4Sb_{12}$.* Mater. Res. Soc. Symp. Proc., 2010. **1267**: p. DD05-25.

88. H. Li, X. F. Tang, X. L. Su, and Q.J. Zhang, *Preparation and thermoelectric properties of high-performance Sb additional $Yb_{0.2}CoSb_{12+y}$ bulk materials with nanostructures.* Appl. Phys. Lett., 2008. **92**(20): p. 202114 (1-3).

89. X. F. Tang, W. J. Xie, H. Li, W. Y. Zhao, and Q.J. Zhang, *Preparation and thermoelectric transport properties of high-performance p-type Bi_2Te_3 with layered nanostructure.* Appl. Phys. Lett., 2007. **90**(1): p. 012102 (1-3).

90. W. J. Xie, X. F. Tang, Y. G. Yan, Q. J. Zhang, and T. M. Tritt, *High thermoelectric performance BiSbTe alloy with unique low-dimensional structure.* J. Appl. Phys., 2009. **105**(11): p. 113713 (1-8).

91. W. J. Xie, X. F. Tang, Y. G. Yan, Q. J. Zhang, and T. M. Tritt, *Unique nanostructures and enhanced thermoelectric performance of melt-spun BiSbTe alloys.* Appl. Phys. Lett., 2009. **94**(10): p. 102111 (1-3).

92. Q. Jie, J. Zhou, X. Shi, I. Domitriv, and Q. Li, *Impact of grain boundaries on the thermoelectric properties of non-equilibrium synthesized p-type $Ce_{1.05}Fe4Sb_{12.04}$ filled skutterudites with nanostructure.* Unpublished work, 2010.

93. B. Cantor, W. T. Kim, B. P. Bewlay, and A. G. Gillen, *Microstructure-cooling rate correlations in melt-spun alloys.* J. Mater. Sci, 1991. **26** p. 1266-1276.